Order-by-disorder and spin-orbital liquids in a distorted Heisenberg-Kitaev model

Eran Sela,[1] Hong-Chen Jiang,[2] Max H. Gerlach,[3] and Simon Trebst[3]
[1]*Raymond and Beverly Sackler School of Physics and Astronomy, Tel-Aviv University, Tel Aviv, 69978, Israel*
[2]*Department of Physics, University of California, Berkeley, California 94720, USA*
[3]*Institute for Theoretical Physics, University of Cologne, 50937 Cologne, Germany*
(Received 24 April 2014; revised manuscript received 18 June 2014; published 14 July 2014)

The microscopic modeling of spin-orbit entangled $j = 1/2$ Mott insulators such as the layered hexagonal iridates Na_2IrO_3 and Li_2IrO_3 has spurred an interest in the physics of Heisenberg-Kitaev models. Here we explore the effect of lattice distortions on the formation of the collective spin-orbital states that include not only conventionally ordered phases but also gapped and gapless spin-orbital liquids. In particular, we demonstrate that in the presence of distortions, i.e., spatial anisotropies of the exchange couplings, conventionally ordered states are formed through an order-by-disorder selection, which is not only sensitive to the type of exchange anisotropy but also to the relative strength of the Heisenberg and Kitaev couplings. The spin-orbital liquid phases of the Kitaev limit—a gapless phase in the vicinity of spatially isotropic couplings and a gapped Z_2 phase for a dominant spatial anisotropy of the exchange couplings—show vastly different sensitivities to the inclusion of a Heisenberg exchange. While the gapless phase is remarkably stable, the gapped Z_2 phase quickly breaks down in what might be a rather unconventional phase transition driven by the simultaneous condensation of its elementary excitations.

DOI: 10.1103/PhysRevB.90.035113 PACS number(s): 75.10.Jm, 71.20.Be, 75.25.Dk, 75.30.Et

I. INTRODUCTION

The intricate interplay of electronic correlations, spin-orbit coupling, and crystal-field effects in $5d$ transition metal oxides has led to the discovery of an intriguing variety of quantum states of matter including Weyl semimetals, axion insulators, or topological Mott insulators [1]. In the correlation-dominated regime, unusual local moments such as spin-orbit entangled degrees of freedom can form and whose collective behavior gives rise to unconventional types of magnetism including the formation of quadrupolar correlations or the emergence of so-called spin liquid states [2]. On the materials side, a particularly prolific group of compounds are the iridates, whose electronic state can be either weakly conducting or insulating. Common to all iridates is that the iridium ions typically occur in an Ir^{4+} ionization state corresponding to a $5d^5$ electronic configuration. For the insulating compounds, a particularly intriguing scenario is the formation of a so-called $j = 1/2$ Mott insulator [3,4], in which a crystal field splitting of the d orbitals into t_{2g} and e_g orbitals and a subsequent spin-orbit entanglement leads to a Mott transition yielding a completely filled $j = 3/2$ state and a half-filled $j = 1/2$ doublet. The microscopic exchange between these spin-orbit entangled $j = 1/2$ local moments has been argued [5,6] to give rise to interactions which combine a spinlike contribution in form of an isotropic Heisenberg exchange with an orbital-like contribution in form of a highly anisotropic exchange whose easy axis depends on the spatial orientation of the exchange path. Such orbital exchange interactions are well known from the early work of Kugel and Khomskii [7] on quantum compass models [8] to induce a high level of exchange frustration, i.e., they inhibit an ordering transition of the local moments that cannot simultaneously align with all their nearest neighbors due to the competing orientations of the respective easy axis. This frustration mechanism is particularly effective in the so-called Kitaev model [9], a honeycomb compass model where the exchange easy axis points along the x, y, and z directions for the three different bond orientations in the honeycomb lattice, see Fig. 1(b). Its phase diagram parametrized in the relative coupling strength of the three types of exchanges exhibits two incarnations of spin liquid phases: an extended gapless spin liquid phase around the point of equally strong exchange interactions and gapped Z_2 spin liquid phases if one of the three coupling strengths dominates, see Fig. 1(c) for a detailed phase diagram. On the materials side, the layered iridates Na_2IrO_3 and Li_2IrO_3, which form $j = 1/2$ Mott insulators with the iridium ions arranged on a hexagonal lattice as illustrated in Fig. 1(a), have recently attracted considerable attention as possible solid state incarnations [5,6,10–13] of the Heisenberg-Kitaev model.[1]

In this manuscript, we inspect the role of distortions on the collective spin-orbital state of the hexagonal Heisenberg-Kitaev model away from the exactly solvable Kitaev limit. The distortions are realized in the form of spatial anisotropies of the strength of the exchange interactions, which are varied on bonds along one of the three principal lattice directions with respect to the other two. Our motivation to do so has been twofold. First, early space group determinations of the layered iridate Na_2IrO_3 using powder x-ray diffraction scans [10] hinted at space group C2/c, in which the hexagonal lattice formed by the Ir^{4+} ions is slightly distorted along one of its three principal directions. However, more refined inelastic neutron scattering [12] and single-crystal x-ray diffraction measurements [13] later revealed that the correct space group of Na_2IrO_3 is in fact space group C2/m and the hexagonal lattice formed by the Ir^{4+} ions is an almost perfectly 120° symmetric honeycomb lattice. As we will show in this manuscript, the collective spin-orbital states of these systems

[1]Generalizations of the Heisenberg-Kitaev model to lattice geometries beyond the hexagonal lattice have recently been considered in both two and three spatial dimensions [50–57] motivated in part by the recent synthesis of three-dimensional honeycomb iridates [58,59].

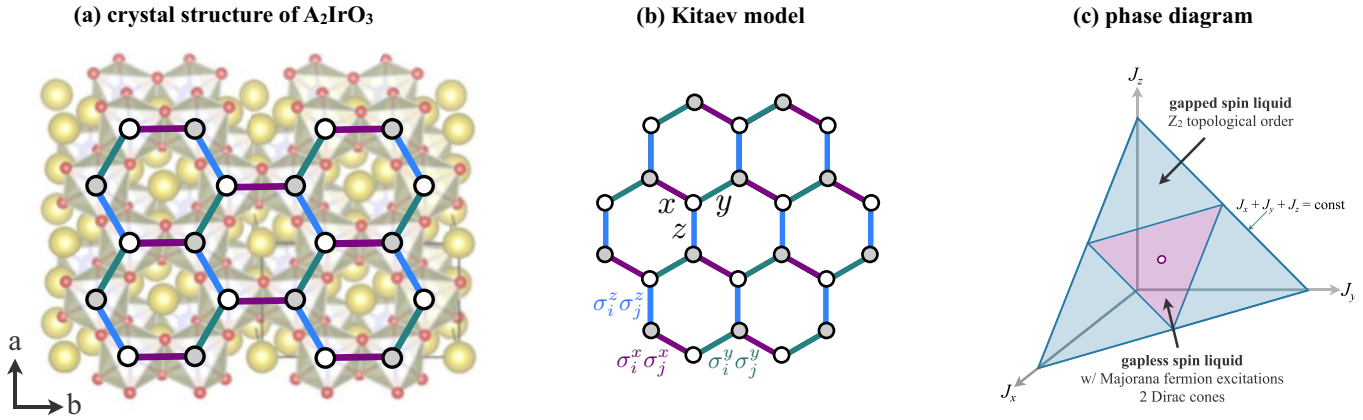

FIG. 1. (Color online) (a) Crystal structure of the layered iridates A_2IrO_3 with A = Na, Li. (b) Sketch of the microscopic interactions in the Kitaev honeycomb model. (c) Phase diagram of the quantum Kitaev model.

are nevertheless highly sensitive to small spatial anisotropies of the exchange couplings, which experimentally can be probed via external pressure measurements inducing small lattice distortions and concurrent exchange anisotropies. Second, we hoped to shed further light on the putative quantum critical point in the undistorted Heisenberg-Kitaev model [6,14–16] between a gapless spin-orbital liquid phase extending out of the Kitaev limit and a conventionally ordered "stripy" phase for the intermediate regime of roughly equally strong Heisenberg and Kitaev couplings. Our analysis shows that exchange coupling distortions are relevant perturbations in any field theoretical description of such a quantum critical point, which depending on their relative strength induce different types of conventionally ordered states in an order-by-disorder selection. This mechanism, which for an infinitesimally small distortion selects a subset of the six possible stripy spin-orbital orderings of the undistorted model, is at play for the entire stripy phase of the Heisenberg-Kitaev model in the intermediate coupling regime. In fact, the selection process turns out to be subtly sensitive not only on the sign of the distortion but also the relative coupling strength of Heisenberg and Kitaev exchange, which leads to a total of four different stripy-ordered phases in the phase diagram of the distorted Heisenberg-Kitaev model.

We will start our discussion by first considering the classical variant of the distorted Heisenberg-Kitaev model in Sec. II. The phase diagram of the classical model already includes all of the conventionally ordered phases found in its quantum mechanical counterpart as well as its own variation of an order-by-disorder selection of ordered states in the presence of exchange coupling distortions. The entire phase diagram of the classical model as well as its finite-temperature behavior are discussed via extensive numerical simulations. We further consider in detail the classical limit of the Kitaev model, which in the absence of distortions is known to exhibit a classical spin liquid state with Coulomb gas correlations [17]. We show that the inclusion of exchange distortions leads to a break-down of these power-law correlations and a partial lifting of the residual entropy at zero-temperature, which is also reflected in characteristic signatures of the low-temperature specific heat behavior. We then turn to the quantum Heisenberg-Kitaev model in Sec. III whose phase diagram we have determined via extensive numerical simulations relying on the density matrix renormalization group (DMRG) on finite two-dimensional clusters. The quantum order-by-disorder selection is discussed and found to be in perfect agreement with the numerical data. Finally, we discuss the possibility of an exotic continuous quantum phase transition, where the Heisenberg exchange drives the system out of the gapped Z_2 spin liquid phase of the distorted Kitaev model into a stripy-ordered phase. Based on perturbative arguments, we conjecture that this transition might be driven by the simultaneous condensation of the excitations of the Z_2 spin liquid. We round off the manuscript with a summary and outlook in Sec. IV.

II. CLASSICAL HEISENBERG-KITAEV MODEL

We start our discussion of the distorted Heisenberg-Kitaev model by first considering its classical version. Its Hamiltonian is given by

$$\begin{aligned} H &= (1-\alpha)\mathcal{H}_{\text{Heisenberg}} - 2\alpha\mathcal{H}_{\text{Kitaev}} \\ &= \sum_{\langle ij\rangle,\gamma} J_\gamma \left[(1-\alpha)\,\mathbf{S}_i\mathbf{S}_j - 2\alpha\, S_i^\gamma S_j^\gamma\right], \end{aligned} \tag{1}$$

where the spins $\mathbf{S}$ are classical O(3) Heisenberg spins and the sums run over nearest-neighbor bonds $\langle ij\rangle$ along the three principal directions γ of the honeycomb lattice labeled x, y, and z, see Fig. 1(b). The coupling constants $0 < J_\gamma$ parameterize the overall strength of the couplings along these three bonds, while the parameter $0 < \alpha < 1$ parameterizes the relative strength of the Heisenberg and Kitaev exchange with $\alpha = 0$ corresponding to the Heisenberg limit and $\alpha = 1$ corresponding to the Kitaev limit. Note that the Heisenberg exchange is always antiferromagnetic, while the Kitaev exchange is always ferromagnetic. The choice of these coupling signs is motivated by the microscopic modeling [6] of the layered iridate compounds Na_2IrO_3 and Li_2IrO_3. To be even more explicit, the Hamiltonian can be decomposed into three types of bond terms, which read

$$\begin{aligned} H_{ij}^x &= J_x\big[(1-\alpha)\mathbf{S}_i\mathbf{S}_j - (2\alpha)S_i^x S_j^x\big], \\ H_{ij}^y &= J_y\big[(1-\alpha)\mathbf{S}_i\mathbf{S}_j - (2\alpha)S_i^y S_j^y\big], \\ H_{ij}^z &= J_z\big[(1-\alpha)\mathbf{S}_i\mathbf{S}_j - (2\alpha)S_i^z S_j^z\big]. \end{aligned} \tag{2}$$

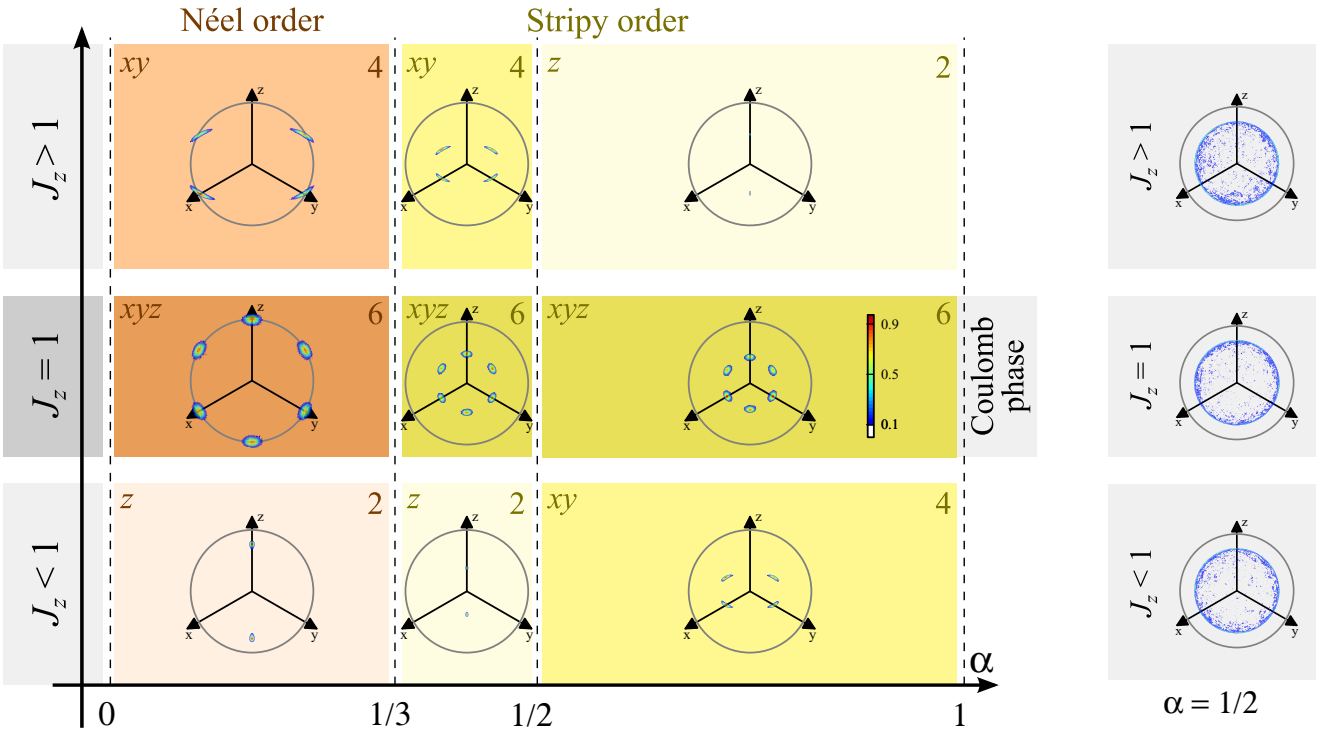

FIG. 2. (Color online) Low-temperature phase diagram of the Heisenberg-Kitaev model under variation of the relative strength α of the Heisenberg and Kitaev couplings and the distortion J_z. For $0 < \alpha < 1/3$, we additionally show histograms of the Néel magnetization $\mathbf{m}_N$, while the histograms for $1/3 < \alpha < 1/2$ and $1/2 < \alpha < 1$ display the stripy order parameter $\mathbf{m}_S$. In the undistorted case with $J_z = 1$, the magnetization vector lies on one of the cubic axes, either in positive or negative direction, yielding a sixfold degeneracy. In the distorted models with $J_z \gtrless 1$ depending on α, there is either a twofold degeneracy with the magnetization pointing in $\pm z$ directions or a fourfold degeneracy where the magnetization points in one of the $\pm x$ or $\pm y$ directions. The color coding is according to a normalization by highest density. Each histogram has been measured in a single parallel-tempering simulation of a system of size $L = 32$. At $\alpha = 1/2$ the model is O(3) symmetric and hence we find no preferred directions of ordering in the $\mathbf{m}_S$-histograms (right-hand side).

The case of $J_x = J_y = J_z$ corresponds to spatially isotropic coupling strengths and the model reflects the C_3 rotational symmetry of the honeycomb lattice. We refer to this case as the undistorted Heisenberg-Kitaev model. To consider the effect of distortions, i.e., spatially anisotropic coupling strengths, we will vary the relative strength of the J_z bond exchange while keeping the other two coupling strengths equal, i.e., $J_x = J_y$. We further use the convention that the overall coupling strength is constant, i.e., $J_x + J_y + J_z = 3$, so that for varying $0 < J_z < 3$, we have $J_x = J_y = (3 - J_z)/2$.

A. Phase diagram of the distorted HK model

A summary of the low-temperature ordered states of this classical model is provided in the phase diagram of Fig. 2. The model exhibits a number of conventionally ordered states which we will discuss in the following.

We start by surveying the phases of the undistorted, C_3 symmetric model for $J_z = 1$, see the center row of Fig. 2. At $\alpha = 0$, we have an antiferromagnetic Heisenberg interaction stabilizing a Néel ordered phase with a staggered moment pointing along an arbitrary direction. Including a small (ferromagnetic) Kitaev interaction lowers the continuous O(3) symmetry of the Heisenberg model to a set of discrete symmetries including (i) time reversal symmetry, (ii) a $2\pi/3$ spin rotation about the [111] spin axis along with C_3 lattice rotations about an arbitrary site, and (iii) an inversion symmetry around any plaquette or bond center. Yet the Néel order survives. Interestingly, the direction of the Néel staggered moment is determined by a classical order-by-disorder mechanism, which we will discuss in more detail in Sec. II B. Upon further increasing the Kitaev exchange, the system will eventually disfavor Néel order and undergo a first-order transition to an alternate ordered state exhibiting "stripy" order. To see the order of the resulting phase, fortunately, at $\alpha = 1/2$ after an appropriate change of spin variables the Hamiltonian reduces again to an O(3) symmetric model, albeit a ferromagnetic one [6].

We briefly describe the four-sublattice basis transformation. Note that at $\alpha = 1/2$, the spin-spin interactions between x, y, and z spin components have equal magnitude but depending on the bond type two interactions are antiferromagnetic and one is ferromagnetic. This interaction can be transformed to a fully ferromagnetic one upon a relative π rotation of the two spins around the special axis. We denote the new spin variables by $\tilde{\mathbf{S}}$. Explicitly, to make this transformation on the full lattice we define a 16 site supercell with sites of types 0,1,2,3 as depicted in Fig. 3. The new spin variables $\tilde{\mathbf{S}}$ are obtained by a π rotation around x, y, or z for sites of type 1, 2, and 3, respectively, and they are simply equal to $\mathbf{S}$ on sites of type 0.

After the four-sublattice basis transformation, the Hamiltonian bond terms in the new spin variables

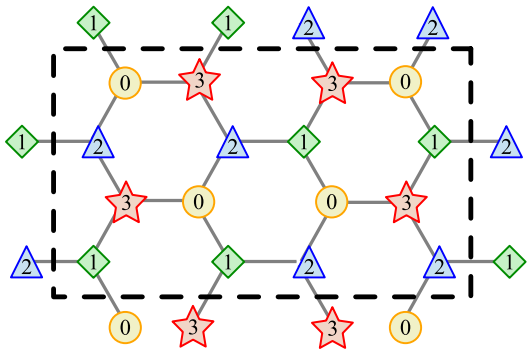

FIG. 3. (Color online) 16 site supercell used to transform the Hamiltonian at $\alpha = 1/2$ to a O(3) symmetric ferromagnetic one. Note that we use a smaller unit cell compared to Ref. [3].

read [6]

$$H^x_{ij} = J_x\left[(\alpha-1)\tilde{\mathbf{S}}_i\tilde{\mathbf{S}}_j + 2(1-2\alpha)\tilde{S}^x_i\tilde{S}^x_j\right],$$
$$H^y_{ij} = J_y\left[(\alpha-1)\tilde{\mathbf{S}}_i\tilde{\mathbf{S}}_j + 2(1-2\alpha)\tilde{S}^y_i\tilde{S}^y_j\right],$$
$$H^z_{ij} = J_z\left[(\alpha-1)\tilde{\mathbf{S}}_i\tilde{\mathbf{S}}_j + 2(1-2\alpha)\tilde{S}^z_i\tilde{S}^z_j\right]. \quad (3)$$

Thus we see that at $\alpha = 1/2$ the system has O(3) symmetry. The ground state is a ferromagnet in the $\tilde{S}$ variables. This translates to the stripy phases of the original spins; see Fig. 4. Similar to the Heisenberg point at $\alpha = 0$, also at $\alpha = 1/2$, the direction of the ferromagnetic moment is arbitrary due to the O(3) symmetry. But any finite deviation from $\alpha = 1/2$ breaks the continuous symmetry down to a discrete one and we expect the ferromagnetic magnetization direction to be fixed at one of few discrete possibilities. As will be seen in Sec. II B, this happens by a classical order by disorder mechanism. The Néel and stripy phases have direct analogs in the quantum case. The most interesting quantum phase occurring for $\alpha \to 1$, which is a spin liquid with gapless excitations in the form of emergent Majorana fermions, does not have an immediate classical analog. Instead, the system forms a classical spin liquid state—a so-called Coulomb gas [17], which exists only

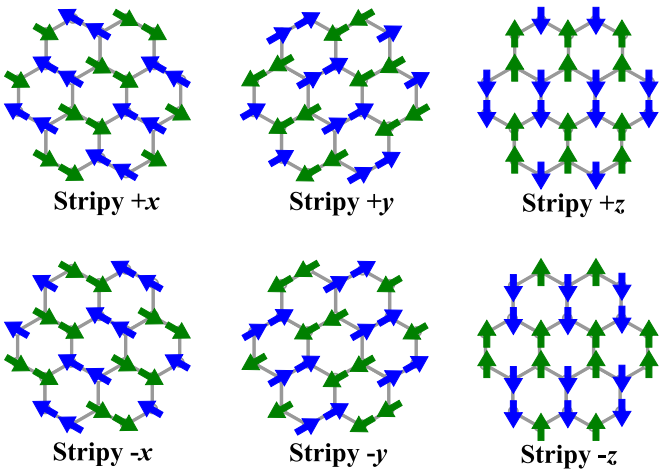

FIG. 4. (Color online) Illustration of the stripy x, y, and z phases where the arrows indicate the spin alignment along the x, y, and z spin directions.

in the Kitaev limit, i.e., $\alpha = 1$, to which we will devote special attention in Sec. II D.

We now consider a finite amount of distortion $J_z \neq 1$. $J_z > 1$ corresponds to strong dimers, while $J_z < 1$ corresponds to dominating chains. As can be easily obtained by calculating the energies of the various ordered states discussed, the Néel ordered region splits up into one ($J_z > 1$) in which spins are in the xy plane and another one ($J_z < 1$) at which they point along the z direction. Also in the stripy phases, spins either point along z for $(\alpha - 1/2)(J_z - 1) > 0$, or they lie in the xy plane for $(\alpha - 1/2)(J_z - 1) < 0$. Note that from pure energetics, the directions of the spins in the xy plane are not fixed. Also here, the finite-temperature order by disorder mechanism comes to play; see Sec. II B.

The paragraph above relies on a simple evaluation of the energy per unit cell of states with perfect Néel or stripy order in direction γ, where spins have the orientations $\pm\hat{\mathbf{e}}_\gamma$. For the Néel states, we sum over Eq. (2) for the three bonds γ' of a unit cell, where $\mathbf{S}_i\mathbf{S}_j = -1$, while the Kitaev term only gives a contribution for the γ bond: $S^{\gamma'}_i S^{\gamma'}_j = -\delta_{\gamma,\gamma'}$. For the stripy states, we sum over Eq. (3) with $\tilde{\mathbf{S}}_i\tilde{\mathbf{S}}_j = 1$ and $\tilde{S}^{\gamma'}_i\tilde{S}^{\gamma'}_j = \delta_{\gamma,\gamma'}$. Thus we find

$$E_{\text{Néel}\,z\,\gamma} = -J_\gamma(1-3\alpha) - \sum_{\gamma'\neq\gamma} J_{\gamma'}(1-\alpha),$$
$$E_{\text{stripy}\,\gamma} = J_\gamma(1-3\alpha) + \sum_{\gamma'\neq\gamma} J_{\gamma'}(\alpha-1). \quad (4)$$

Also the Néel-stripy phase transition lines can be found by equating energies. From

$$E_{\text{Néel}\,z} = E_{\text{stripy}\,z}, \quad (5)$$

we obtain $\alpha = 1/3$, giving the line boundary between Néel and stripy for $J_z < 1$. By comparing

$$E_{\text{Néel}\,xy} = E_{\text{stripy}\,xy}, \quad (6)$$

we also obtain $\alpha = 1/3$, giving the line boundary between Néel and stripy phases for $J_z > 1$. As a result there is a straight vertical line at $\alpha = 1/3$ marking the Néel-stripy transition in the low-temperature phase diagram of Fig. 2.

In Secs. II B and II C, we show that for $J_z \neq 1$ the stripy-ordered phases have different discrete symmetries left and right of the $\alpha = 1/2$ line in Fig. 2. Consequently, this line marks first-order transitions for both $J_z > 1$ and $J_z < 1$. As outlined in Sec. II C, we numerically obtain the finite-temperature phase diagram shown in Fig. 5.

B. Order by disorder and effective Ginzburg-Landau theory

At $\alpha = 1/2$, the magnetization points along an arbitrary direction due to the O(3) symmetry explicitly apparent in Eq. (3) (we refer to the $\tilde{\mathbf{S}}$ variables in terms of which the Hamiltonian is ferromagnetic). At finite deviations from this symmetric point, one expects the Kitaev anisotropic interactions to stabilize a discrete set of orientations of the magnetization. However, as Eq. (4) shows, on the mean-field level, all uniform ferromagnetic states in the O(3) order parameter manifold remain degenerate for $J_z = 1$. Similarly, the mean-field energy in the stripy xy phases is still invariant under continuous rotations in this plane. Along the same lines,

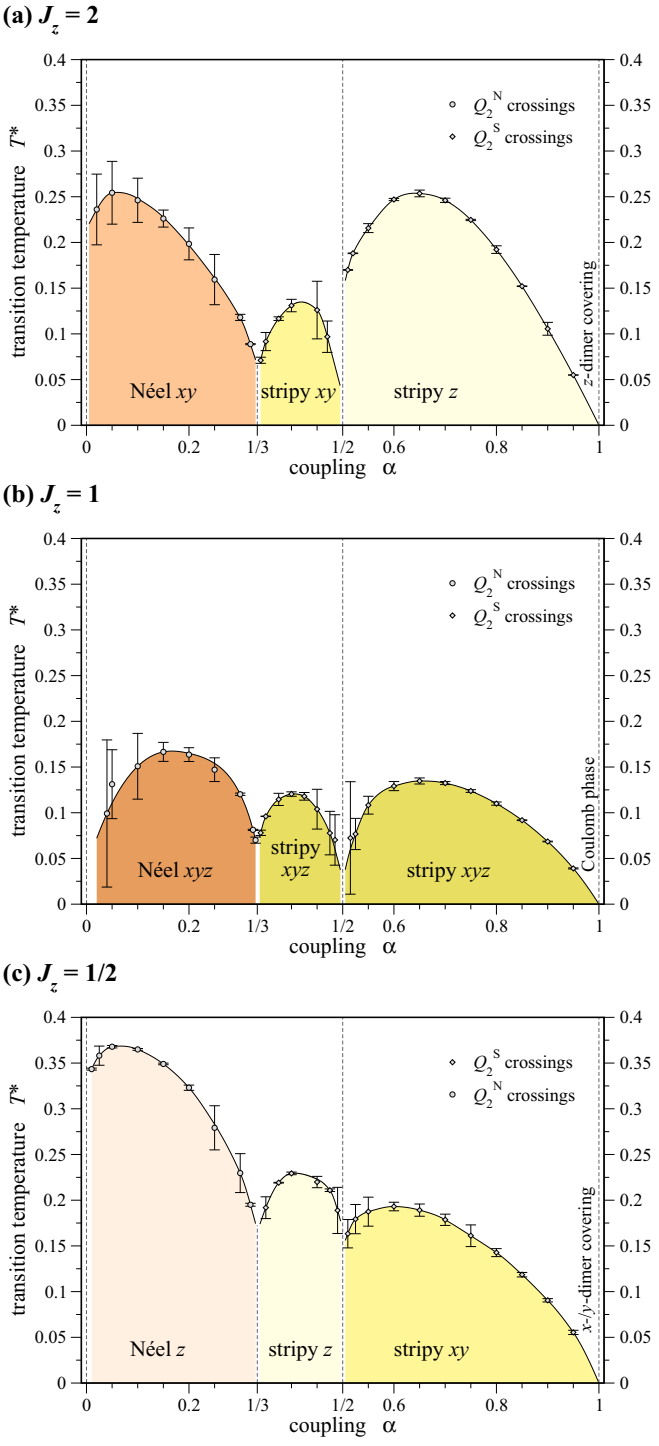

FIG. 5. (Color online) Finite-temperature phase diagrams for (a) $J_z > 1$, (b) $J_z = 1$, and (c) $J_z < 1$. We estimate the temperature of transition to the ordered phase by the intersection point of order parameter Binder cumulant plots $Q_2^{\mathrm{N}}(T)$ for $\alpha < 1/3$ and $Q_2^{\mathrm{S}}(T)$ for $\alpha > 1/3$ averaged over multiple pairs of lattice sizes L. See Fig. 7, for example, data that went into this calculation. The dashed lines at $\alpha = 0, 1/2$ indicate the parameterizations for which the Heisenberg-Kitaev model is O(3) symmetric and as a consequence of the Mermin-Wagner theorem is not expected to display finite-temperature transitions in good agreement with our numerical analysis. The degenerate dimer-covering states at $\alpha = 1$ also do not undergo any phase transition for $T > 0$.

on the mean-field level, the order parameter in the Néel phase for $J_z \geqslant 1$ is not determined.

As we will now see, the Heisenberg-Kitaev model provides a simple example where Villain's order by disorder mechanism comes into play and restricts the order parameter to lie in a subspace of the degenerate manifold. This mechanism requires finite temperatures, where entropic contributions to the free energy become effective. The formal procedure followed below is to integrate out the leading thermal fluctuations, and see that for certain directions of the ordered moment those fluctuations are softer and can further lower the free energy.

We shall consider explicitly the stripy region in terms of the $\tilde{\mathbf{S}}$ variables. We introduce a slowly varying ferromagnetic order parameter field $\langle \tilde{\mathbf{S}}_i \rangle \to \mathbf{M}(\mathbf{r})$ of unit length

$$[M^x(\mathbf{r})]^2 + [M^y(\mathbf{r})]^2 + [M^z(\mathbf{r})]^2 = 1 \tag{7}$$

and define gradients along the directions of the three bonds, $\nabla_{\hat{\mathbf{u}}_\gamma} = \hat{\mathbf{u}}_\gamma \cdot \boldsymbol{\nabla}$, $(\gamma = x, y, z)$, where $\boldsymbol{\nabla} = (\partial_x, \partial_y)$, with unit vectors $\hat{\mathbf{u}}_z = \hat{\mathbf{y}}$ and $\hat{\mathbf{u}}_{x,y} = \mp\frac{\sqrt{3}}{2}\hat{\mathbf{x}} - \frac{1}{2}\hat{\mathbf{y}}$. We set the length of these bonds to unity such that the hexagon area is $A_{\mathrm{hex}} = 3^{3/2}/2$ and the area of the Brilloiuin zone is $A_{BZ} = 4\pi/\sqrt{3}$. Expanding the spin-spin interaction Eq. (3) up to second order in gradients, we obtain the continuum Hamiltonian $H = \int \frac{d^2r}{A_{\mathrm{hex}}} \mathcal{H}[\mathbf{M}]$, with

$$\mathcal{H}[\mathbf{M}] = \sum_\gamma \frac{J_\gamma}{2} [(1-\alpha)(\nabla_{\hat{\mathbf{u}}_\gamma} \mathbf{M})^2 + 2(2\alpha - 1)(\nabla_{\hat{\mathbf{u}}_\gamma} M^\gamma)^2]. \tag{8}$$

For simplicity, we focus on the case $J_x = J_y = J_z = J$.

We now consider the partition function of the continuum model Eq. (8),

$$Z = \int \mathcal{D}\mathbf{M}(\mathbf{r}) e^{-\mathcal{H}[\mathbf{M}(\mathbf{r})]/T}. \tag{9}$$

We proceed by describing the magnetization $\mathbf{M}(\mathbf{r})$ in terms of fluctuations corresponding to two Goldstone modes $\pi_1(\mathbf{r})$ and $\pi_2(\mathbf{r})$ around a uniform magnetization $\hat{\mathbf{e}}$,

$$\mathbf{M}(\mathbf{r}) = \hat{\mathbf{e}}\sqrt{1 - \bar{\pi}^2(\mathbf{r})} + \sum_{a=1,2} \hat{\mathbf{e}}_a \pi_a(\mathbf{r}). \tag{10}$$

Here, $\bar{\pi} = \sqrt{\pi_1^2(\mathbf{r}) + \pi_2^2(\mathbf{r})}$, and the set of unit vectors $\{\hat{\mathbf{e}}_1, \hat{\mathbf{e}}_2, \hat{\mathbf{e}}\}$ forms an orthonormal basis. This allows to rewrite the partition function as

$$Z = \int \mathcal{D}\hat{\mathbf{e}} \int \mathcal{D}\pi_a(\mathbf{r}) e^{-\mathcal{H}[\hat{\mathbf{e}}, \pi_a(\mathbf{r})]/T} = \int \mathcal{D}\hat{\mathbf{e}} e^{-H_{\mathrm{eff}}[\hat{\mathbf{e}}]/T}, \tag{11}$$

hence introducing an effective Hamiltonian of $\hat{\mathbf{e}}$ by integrating over the fluctuations,

$$e^{-H_{\mathrm{eff}}[\hat{\mathbf{e}}]/T} = \int \mathcal{D}\pi_a(\mathbf{r}) e^{-\mathcal{H}[\hat{\mathbf{e}}, \pi_a(\mathbf{r})]/T}. \tag{12}$$

In Appendix A, we compute $H_{\mathrm{eff}}[\hat{\mathbf{e}}]$ explicitly by expanding $\mathcal{H}[\hat{\mathbf{e}}, \pi_a(\mathbf{r})]$ up to quadratic order in the fluctuations $\pi_a(\mathbf{r})$. Up to a constant and up to quadratic order in $2\alpha - 1$, we obtain the symmetry allowed anisotropic term

$$\frac{H_{\mathrm{eff}}}{NT} = -\frac{2}{3}(2\alpha - 1)^2 [(\hat{e}^x)^4 + (\hat{e}^y)^4 + (\hat{e}^z)^4]. \tag{13}$$

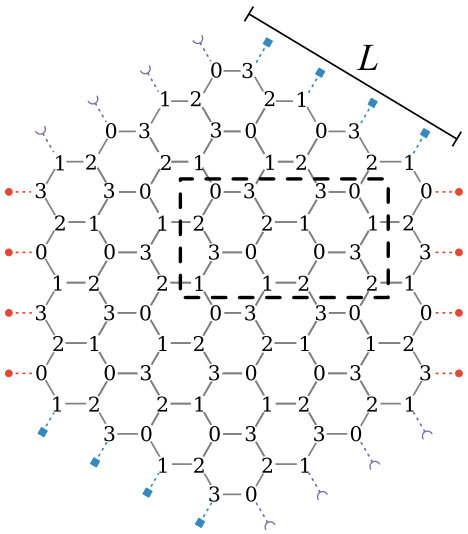

FIG. 6. (Color online) $L = 4$ example of the finite lattices used in our Monte Carlo simulations, where opposing boundaries are periodic as indicated. The numbers show the division into the sublattices used in the definition of the order parameter $\mathbf{m}_S$ in Eq. (14), which matches the supercell in Fig. 3.

This is the main result of this section. Its negative sign restricts the magnetization in the stripy phase to lie along one of the cubic axes. This term is quadratic in $\alpha - 1/2$, implying the same conclusion for both sides of the point $\alpha = 1/2$ in the phase diagram at $J_z = 1$. Similarly, in the stripy xy phases, by the same argument, the magnetization is restricted to either the x or y cubic axes. On the classical level the Néel ordered phase has an equivalent description as the ferromagnet, and our order by disorder calculation implies that the Néel order parameter is restricted to point along one of the cubic axes.

C. Numerical results

Our analysis of the classical Heisenberg-Kitaev model is complemented by an extensive finite-temperature Monte Carlo study. In our simulations, the classical spins $\mathbf{S}_i$ are situated on the vertices of hexagon-shaped clusters with periodic boundary conditions, which realize the C_3 symmetry of the honeycomb lattice and allow to observe unbiasedly all possible orientations in the stripy phases; see Fig. 6. A cluster with a side length of L plaquettes contains $N = 6L^2$ sites.

We apply the standard Metropolis algorithm [18,19] with two different types of proposed moves. In one lattice sweep, we first perform local updates of each individual spin, where the new orientation is chosen from an angular region around the old orientation, which has been tuned in such a way during thermalization that acceptance ratios of 50% are maintained at all temperatures. In a second stage, we then propose $3N$ "bond-flip" moves. In one of these moves, we choose a random pair of nearest-neighbor sites together with their associated bond-direction $\langle i,j\rangle^\gamma$. Then for the spins at both sites we reverse the sign of the spin-component linked via that bond in the Kitaev interaction: $S_i^\gamma \to -S_i^\gamma$ and $S_j^\gamma \to -S_j^\gamma$, whereas the other components are not modified. While the bond-flip update would not be ergodic on its own, in combination with the single-spin update it greatly accelerates simulation dynamics in the stripy phases, vastly facilitating equilibration.

To further improve ergodicity, we combine these canonical updates with a parallel-tempering scheme [20,21]. Here we simulate multiple replicas of the spin system concurrently at different temperatures and exchange configurations between them in a controlled manner that satisfies detailed balance. In this way, short autocorrelation times at high temperatures can be exploited to easily overcome free energy barriers at low temperatures, and we can reach all relevant regions of phase space in a single simulation regardless of initial conditions.

We measure two vector order parameters to distinguish between different antiferromagnetic spin alignments:

$$\mathbf{m}_N = \frac{1}{N}\left(\sum_{i\in a}\mathbf{S}_i - \sum_{i\in b}\mathbf{S}_i\right) \quad \text{and}$$

$$\mathbf{m}_S = \frac{1}{2N}\left(\sum_{i\in 0}\mathbf{S}_i + \sum_{i\in 1}\mathbf{S}_i - \sum_{i\in 2}\mathbf{S}_i + \sum_{i\in 3}\mathbf{S}_i\right). \tag{14}$$

Here, a and b stand for the two sublattices of the honeycomb lattice, while the four honeycomb sublattices formed by the sites of the different types of the supercell of Fig. 3 are denoted by 0, 1, 2, and 3. Figure 6 shows how these sublattices are assigned in our finite lattices. $|\mathbf{m}_N| = 1$ corresponds to perfect Néel order, while $|\mathbf{m}_S| = 1$ is realized for perfect stripy order. The preferred orientations of the magnetization vectors $\mathbf{m}_N$ and $\mathbf{m}_S$ reflect which ordering directions are possible in the different Néel and stripy phases. In Eq. (14),we have chosen an asymmetric definition of the order parameter $\mathbf{m}_S$, where one of the sublattice magnetizations is counted negative and three are counted positive. With this definition $\mathbf{m}_S$ is simultaneously an order parameter for the stripy x, y, and z phases on the same lattice.[2] By measuring histograms of the components of $\mathbf{m}_N$ and $\mathbf{m}_S$, we were able to verify the analytical arguments of Sec. II B. We obtain planar representations of $\mathbf{m}_N$ and $\mathbf{m}_S$ by mapping the three Cartesian basis vectors to the complex plane as in $\hat{\mathbf{e}}_x \to \exp(7i\pi/6)$, $\hat{\mathbf{e}}_y \to \exp(11i\pi/6)$, and $\hat{\mathbf{e}}_z \to \exp(i\pi/2)$ and show the resulting histograms as insets in the phase diagram of Fig. 2. Both the carefully chosen shape of the finite lattices and the parallel-tempering algorithm are essential tools allowing us to fully explore configuration space in our simulations as reflected in these histograms.

Recently, Price and Perkins [22,23] studied the undistorted, C_3-symmetric classical Heisenberg-Kitaev model at finite temperature. Following their analysis, we study the Binder cumulants of the absolute valued order parameters,

$$Q_2^N = 1 - \frac{1}{3}\frac{\langle m_N^4\rangle}{\langle m_N^2\rangle^2} \quad \text{and} \quad Q_2^S = 1 - \frac{1}{3}\frac{\langle m_S^4\rangle}{\langle m_S^2\rangle^2}, \tag{15}$$

in order to pinpoint the precise temperature of the transitions into the ordered phases. At criticality, their values depend only weakly on the system size. Hence the intersection point of

[2]Note that Refs. [22,23] use an alternative definition of the stripy-order parameter, which is specified on a choice of sublattices different from ours.

$Q_2^{\mathrm{N}}(T)$ or $Q_2^{\mathrm{S}}(T)$ curves evaluated for different L gives a good estimate of the critical temperature.

Interestingly, Price and Perkins found that for $\alpha \neq 0, 1/2, 1$, the entrance to the ordered phases (Néel or stripy) from the high-temperature paramagnetic phase undergoes *two* consecutive phase transitions, via a small sliver of a critical Kosterlitz-Thouless phase. In this intermediate phase, the effective model is a six-state clock model, corresponding to the six possible stripy or Néel phases, where an effective U(1) symmetry emerges. However, for the distorted model there are only two or four degenerate stripy or Néel phases. In this case, the intermediate U(1) symmetric phase is not expected [24] and no evidence of it is found in our numerical analysis.

We apply standard multiple histogram reweighting techniques [25,26] to the temperature-sorted observable time series in combination with numerical minimization routines [27] to find the intersection points for systems of different sizes up to $L = 128$. Statistical uncertainties are estimated by performing the entire analysis on jackknife resampled data sets [28]. Plots of Binder cumulants close to their crossing points are given in Fig. 7 for several parameter sets. We average over the results for different values of L to estimate the transition temperatures T^* shown in Fig. 5.

For the symmetric case $J_z = 1$, our approach resolves the lower of the two transition temperatures of the analysis of Ref. [23]. For the distorted model, only a single transition is expected as argued above. We associate this transition with the crossing point of the Binder cumulant curves of different sizes as shown in the examples in Fig. 7.

D. Emergent magnetostatics in the Kitaev limit

Before concluding our discussion of the classical Heisenberg-Kitaev model, we will briefly discuss the physics of the Kitaev limit ($\alpha = 1$). While its quantum mechanical counterpart is well known as a paradigmatic, exactly solvable spin model harboring various spin liquid ground states, the classical Kitaev model certainly deserves some attention as well. In its undistorted form ($J_x = J_y = J_z = 1$), it is one of the simplest, analytically tractable classical spin models that evades a thermal phase transition and harbors a classical spin liquid state, which at zero temperature exhibits an extensive degeneracy and pair correlations decaying with a characteristic power law [17]. These zero-temperature features can be traced back to an effective description in terms of emergent magnetostatics—an example of a so-called Coulomb gas [29]. We will briefly review the arguments showing the origin of this emergent spin liquid in the classical Kitaev model in the following with a more detailed and self-consistent account being given in Appendix B. We then discuss the effect of finite distortions, which lead to a (partial) lifting of the zero-temperature degeneracy and a break-down of the Coulomb correlations. However, characteristic remnants of the Coulomb description remain as signatures in the low-temperature specific heat as we detail in the subsequent section.

As noted earlier, the undistorted classical Kitaev model incorporates a high level of exchange frustration with each spin being subject to competing magnetic exchanges that equally favor alignment along one of the three orthogonal axes of a classical O(3) Heisenberg spin. As one approaches

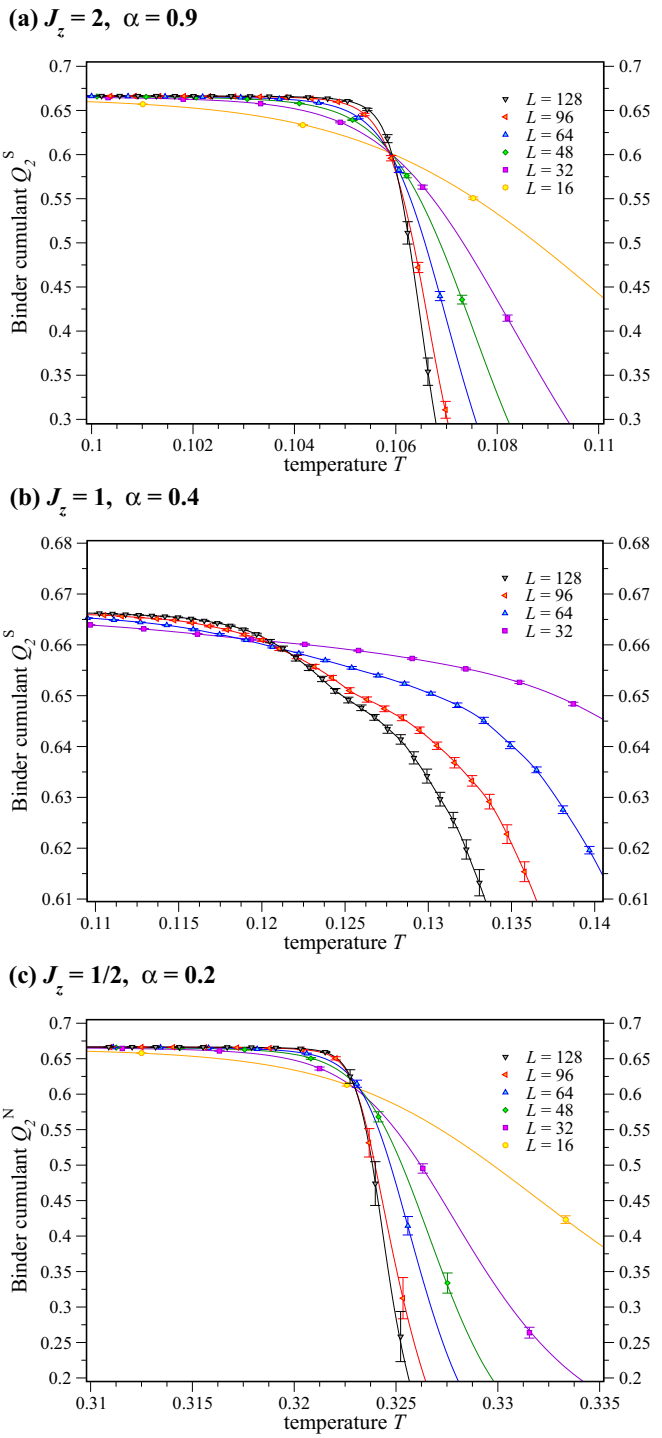

FIG. 7. (Color online) Binder cumulant curves of the order parameter evaluated over T for various system sizes L close to their crossing, which gives an estimate of the transition temperature for several example parameter sets. Shown are the cumulant of $\mathbf{m}_{\mathrm{S}}$ for the transitions to (a) the stripy z and (b) the stripy xyz phases as well as (c) the cumulant of $\mathbf{m}_{\mathrm{N}}$ for the transition to the Néel z phase. Symbols with error bars are single temperature data, while continuous lines are interpolated by multiple histogram reweighting.

the zero-temperature limit of this model, it is easy to see [17] that the total energy of the system can be minimized by spin configurations where spins align in a pairwise fashion along

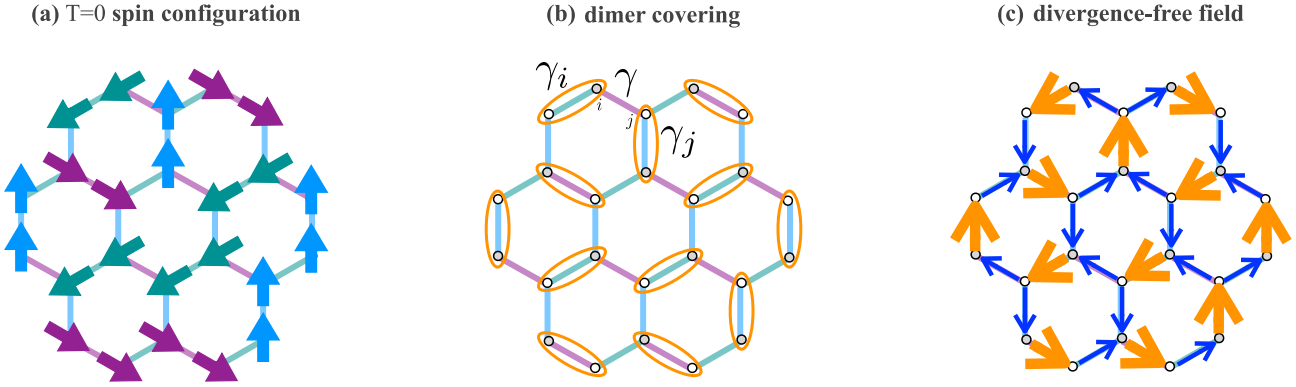

FIG. 8. (Color online) A zero-temperature configuration of the C_3 symmetric Kitaev model is a generic dimer covering state, to which we can associate a divergence-free field.

one of the three easy axes of the magnetic exchange, i.e., the one favored by the bond between the two spins forming a pair. An example of such a spin configuration is illustrated in Fig. 8(a). Since every spin is part of precisely one such aligned pair, we can identify each pair of aligned spins with a "dimer." As a consequence, any such energy minimizing spin configuration can be mapped to a hardcore *dimer covering* of the honeycomb lattice as illustrated in Fig. 8(b) where every site (spin) is part of precisely one dimer. This mapping allows two immediate conclusions. First, it is well known since the early work of Wannier [30], Kasteleyn [31], and Elser [32] that the number of dimer coverings on the hexagonal lattice grows exponentially in the system size and as thus we can immediately estimate the zero-temperature degeneracy of the spin model. Second, it has long been appreciated [29] that the hard-core dimer constraint on a bipartite lattice allows a mapping of any dimer covering to a *divergence-free field* configuration, which is schematically illustrated in Fig. 8(c). It is precisely this description of the zero-temperature spin configurations in terms of a divergence-free magnetic field that allows to draw the connection to an emergent *Coulomb gas* description. The latter is well known to give rise to power-law correlations, which translated back to the original spin model are pair correlations of the form

$$\langle (S_i^z)^2 \cdot (S_{i+r}^z)^2 \rangle \propto \frac{1}{r^2}.$$

For a detailed and self-consistent description of the Coulomb gas formulation of the zero-temperature classical Kitaev model, we refer the reader to Appendix B.

When introducing distortions of the exchange couplings, the extensive degeneracy of zero-temperature states is immediately lifted. For $J_z > 1$, two spin configurations are singled out where spins align along the z direction again in a pairwise fashion—with both states being mapped to an identical dimer covering as illustrated on the left-hand side in Fig. 9. As a consequence, the spin liquid physics disappears entirely and the system undergoes a conventional Z_2 symmetry breaking thermal phase transition into one of the two states. For $J_z < 1$, a different picture emerges. While the extensive zero-temperature degeneracy is still lifted, the system retains a subextensive degeneracy down to zero temperature where the spins align in pair-wise fashion along the zigzag chains spanned by the x and y bonds as illustrated on the right-hand side in Fig. 9. The consequence of this lifting again is the loss of Coulomb correlations, but the system still evades a conventional ordering transition down to zero temperature with characteristic features arising for instance in the specific heat as discussed in the next section.

1. Specific heat and zero modes

One characteristic feature of the extensive manifold of zero-temperature spin configurations is that it gives rise to certain soft fluctuations called *zero modes*. Following the pioneering work of Chalker *et al.* [33], we show in the remainder of this section that these zero modes reduce the specific heat in its $T \to 0$ limit in a universal way—a characteristic signature that as we show can easily be tracked by numerical simulations of the classical spin model.

To start our discussion of the analytical arguments, we consider fluctuations around a given dimer covering or spin configuration, respectively. Each spin i belonging to a dimer on a γ bond gives rise to possible fluctuations in the two directions orthogonal to γ. For example, for a spin belonging to a z dimer and pointing along $+z$, we write

$$\mathbf{S}_i = \left(\epsilon_i^x, \epsilon_i^y, \sqrt{1 - \epsilon_i^{x\,2} - \epsilon_i^{y\,2}}\right). \tag{16}$$

The fluctuations in the x and y directions influence also the z component due to the unit constraint $|\mathbf{S}_i| = 1$.

Let $\mathcal{D}$ denote the set of dimerized bonds. For $\langle i,j \rangle \in \mathcal{D}$ and assuming for simplicity that this is a z type bond, the Kitaev

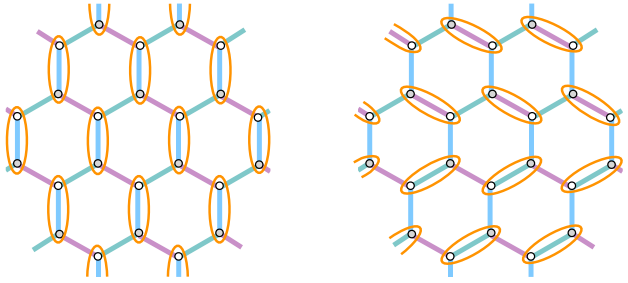

FIG. 9. (Color online) (Left) The preferable dimer covering state for dominating J_z. (Right) Typical dimer covering states for $J_x = J_y > J_z$.

spin-spin interaction reads

$$-J_z S_i^z S_j^z\big|_{\langle i,j\rangle\in\mathcal{D}} = -J_z\sqrt{1-\epsilon_i^{x\,2}-\epsilon_i^{y\,2}}\sqrt{1-\epsilon_j^{x\,2}-\epsilon_j^{y\,2}}$$
$$= -J_z + \frac{J_z}{2}\left(\epsilon_i^{x\,2}+\epsilon_i^{y\,2}+\epsilon_j^{x\,2}+\epsilon_j^{y\,2}\right) + \mathcal{O}(\epsilon^4). \quad (17)$$

We see that up to quadratic order, fluctuations do not interact across dimerized bonds (no $\epsilon_i\epsilon_j$ coupling terms for $\langle i,j\rangle\in\mathcal{D}$). On the other hand, for a nondimerized bond γ [see Fig. 8(b)] the Kitaev interaction reads

$$-J_\gamma S_i^\gamma S_j^\gamma\big|_{\langle i,j\rangle\notin\mathcal{D}} = -J_\gamma\epsilon_i^\gamma\epsilon_j^\gamma. \quad (18)$$

Thus, expanding the Hamiltonian in ϵ to quadratic order, the fluctuation corrections consist of decoupled terms, which live on the nondimerized bonds and read

$$H^{(2)} = \sum_{\langle i,j\rangle_\gamma\notin\mathcal{D}} h\left(\epsilon_i^\gamma,\epsilon_j^\gamma\right), \quad (19)$$

where

$$h\left(\epsilon_i^\gamma,\epsilon_j^\gamma\right) = -J_\gamma\epsilon_i^\gamma\epsilon_j^\gamma + \tfrac{1}{2}\left(J_{\gamma i}\epsilon_i^{\gamma\,2} + J_{\gamma j}\epsilon_j^{\gamma\,2}\right). \quad (20)$$

Interestingly, for $J_x = J_y = J_z$,

$$h\left(\epsilon_i^\gamma,\epsilon_j^\gamma\right) = -\frac{J_z}{2}\left(\epsilon_i^\gamma-\epsilon_j^\gamma\right)^2. \quad (21)$$

This implies the existence of a zero mode: $(\epsilon_i^\gamma+\epsilon_j^\gamma)$ does not appear in $H^{(2)}$. This zero mode has been identified [34] to be a sliding degree of freedom of the dimer covering states. For low enough temperatures, fluctuations become small and the partition function becomes

$$Z \cong \int \mathcal{D}(\{\epsilon\}) e^{-\frac{H^{(2)}(\{\epsilon\})}{T}}. \quad (22)$$

For any quadratic eigenmode ϵ, with energy $E = c_2\epsilon^2$, the contribution to the specific heat then becomes

$$C_v = \frac{d}{dT}\frac{\int d\epsilon (c_2\epsilon^2) e^{-\frac{c_2\epsilon^2}{T}}}{\int d\epsilon e^{-\frac{c_2\epsilon^2}{T}}} = \frac{\int dx x^2 e^{-x^2}}{\int dx e^{-x^2}} = \frac{1}{2}, \quad (23)$$

independent of the coefficient c_2. However, in our system, we have to further consider the contributions of the zero modes. For those modes, we need to go to quartic order, i.e., $E = c_4\epsilon^4$, for which the contribution to the specific heat can be estimated to be

$$C_v = \frac{d}{dT}\frac{\int d\epsilon (c_4\epsilon^4) e^{-\frac{c_4\epsilon^4}{T}}}{\int d\epsilon e^{-\frac{c_4\epsilon^4}{T}}} = \frac{\int dx x^4 e^{-x^4}}{\int dx e^{-x^4}} = \frac{1}{4}, \quad (24)$$

again independent of the coefficient c_4. In a standard state without zero modes (such as a ferromagnetic state), we would have two quadratic modes (ϵ_i^x and ϵ_i^y) per spin. This would give the zero temperature value of the specific heat per spin:

$$C_v^{\text{ferro}}(T\to 0) = \tfrac{1}{2}+\tfrac{1}{2} = 1. \quad (25)$$

However, in the Coulomb phase of the classical Kitaev model, we have only one zero mode for each quadratic mode, hence

$$C_v^{J_z=1}(T\to 0) = \tfrac{1}{2}+\tfrac{1}{4} = \tfrac{3}{4}. \quad (26)$$

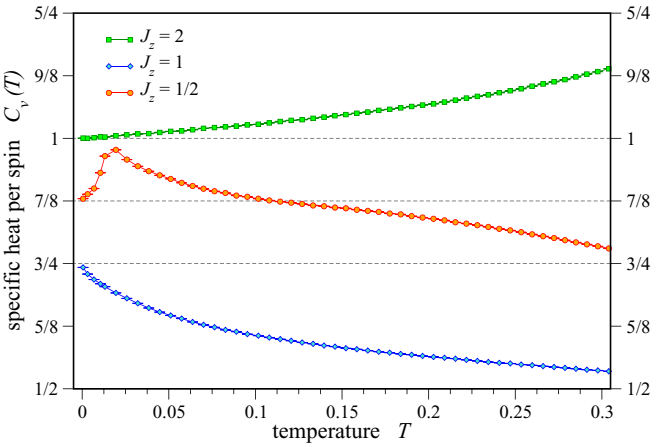

FIG. 10. (Color online) Low-temperature behavior of the specific heat per spin $C_v(T)$ in the classical Kitaev model with different distortions. Shown are Monte Carlo results obtained at temperatures $T \geqslant 1/2000$ demonstrating that in the limit of $T\to 0$, one finds $C_v^{J_z=1}\to 3/4$, $C_v^{J_z>1}\to 1$ and $C_v^{J_z<1}\to 7/8$. The data have been obtained for systems of side length $L = 16$.

We now consider the effect of a finite distortion, i.e., $J_z \neq J_x = J_y$, which splits the degeneracy of the various dimer covering states. For $J_z > J_x = J_y$, namely $J_z > 1$, the dimer covering with only z dimers has the lowest energy (see Fig. 9).

At the same time, fluctuations around this state are described by Eq. (19), which can be written as

$$h\left(\epsilon_i^\gamma,\epsilon_j^\gamma\right) = \frac{3(J_z-1)}{8}\left(\epsilon_i^\gamma+\epsilon_j^\gamma\right)^2 + \frac{J_z+3}{8}\left(\epsilon_i^\gamma-\epsilon_j^\gamma\right)^2. \quad (27)$$

For $J_z > 1$, the two coefficients in this equation are positive, leaving no zero modes. Hence

$$C_v^{J_z>1}(T\to 0) = \tfrac{1}{2}+\tfrac{1}{2} = 1. \quad (28)$$

For $J_z < J_x = J_y$, the dimers cover x or y bonds in the ground state (see Fig. 9). Now consider fluctuations around these 1D covering states. The Hamiltonian for the fluctuations is the same as Eq. (19), but now there are two types of nondimerized bonds. For $\langle i,j\rangle_\gamma\notin\mathcal{D}$ with $\gamma = x$ or y, h has the form of Eq. (21), implying a zero mode. But for $\langle i,j\rangle_\gamma\notin\mathcal{D}$ with $\gamma = z$, the Hamiltonian h has the form of Eq. (27), implying no zero mode. As a result the specific heat per spin becomes

$$C_v^{J_z<1}(T\to 0) = \tfrac{1}{2}\left(\tfrac{1}{2}+\tfrac{1}{4}\right)+\tfrac{1}{2}\left(\tfrac{1}{2}+\tfrac{1}{2}\right) = \tfrac{7}{8}. \quad (29)$$

Our Monte Carlo calculations, summarized in Fig. 10, nicely reproduce these fractions and are thus able to pinpoint the different constraints on the dimer covering states underlying the Coulomb gas.

III. QUANTUM HEISENBERG-KITAEV MODEL

We now turn to a discussion of the quantum version of the distorted Heisenberg-Kitaev model, i.e., we again consider the Hamiltonian

$$H = (1-\alpha)\mathcal{H}_{\text{Heisenberg}} - 2\alpha\mathcal{H}_{\text{Kitaev}}$$
$$= \sum_{\langle ij\rangle,\gamma} J_\gamma\left[(1-\alpha)\,\mathbf{S}_i\mathbf{S}_j - 2\alpha\, S_i^\gamma S_j^\gamma\right], \quad (30)$$

where the spins $\mathbf{S}_i$ are now quantum mechanical SU(2) spin-1/2 degrees of freedom. [In our convention $\mathbf{S}_i$ are represented by Pauli matrices $(S_i^\gamma)^2 = 1$.] The exchange parameter $0 < \alpha < 1$ again interpolates between the antiferromagnetic Heisenberg model ($\alpha = 0$) and the ferromagnetic Kitaev model ($\alpha = 1$) and the distortion of the exchange couplings is parametrized by $0 < J_z < 3$ with the simultaneous conditions that all three spin exchange couplings add up to a constant, i.e., $J_x + J_y + J_z = 3$ and $J_x = J_y$. The case $J_z = 1$ then corresponds to the undistorted situation where the spin exchange along all three bonds has equal magnitude, i.e., $J_x = J_y = J_z$. The limit $J_z = 3$ ($J_x = J_y = 0$) corresponds to decoupled dimers on the z bonds, while the opposite limit of $J_z = 0$ ($J_x = J_y = 3/2$) corresponds to decoupled zigzag chains along the x and y bonds.

When exploring the (α, J_z)-parameter space, we find that the above model not only harbors quantum analogues of all classically ordered states, but exhibits a number of additional genuinely quantum states including a valence-bond solid and two spin-orbital liquid phases, which both extend well beyond the well-studied Kitaev limit of the quantum model. In fact, one of the more interesting features of the extended phase diagram of the quantum Heisenberg-Kitaev model is the possible occurrence of unconventional continuous phase transitions between these gapped and gapless spin-orbital liquid phases and conventionally ordered states.

In the following, we will first discuss the general quantum phase diagram of the distorted Heisenberg-Kitaev model and the numerical simulations underlying its determination and then focus our discussion on the possibly interesting quantum critical behavior associated with the phase transition out of one of the spin-orbital liquid phases.

A. Phase diagram of the quantum model

The phase diagram of the quantum Heisenberg-Kitaev model in the presence of exchange distortions is summarized in Fig. 11. Similar to the classical model, we find an extended Néel ordered phase around the Heisenberg limit which upon distorting the exchange interactions undergoes a quantum order-by-disorder transition locking the spin orientation in the ordered phases to the z (x or y) direction for $J_z < 1$ ($J_z > 1$), respectively. For $J_z \gtrsim 1.35$, the system undergoes a transition into a valence-bond solid (VBS), which adiabatically connects to the limit of isolated dimer singlets on the z bonds in the limit $J_z = 3$ (and $\alpha < 1/2$).

For $\alpha = 1/2$, the quantum model exhibits an SU(2) symmetry that is again rooted in the observation that for this

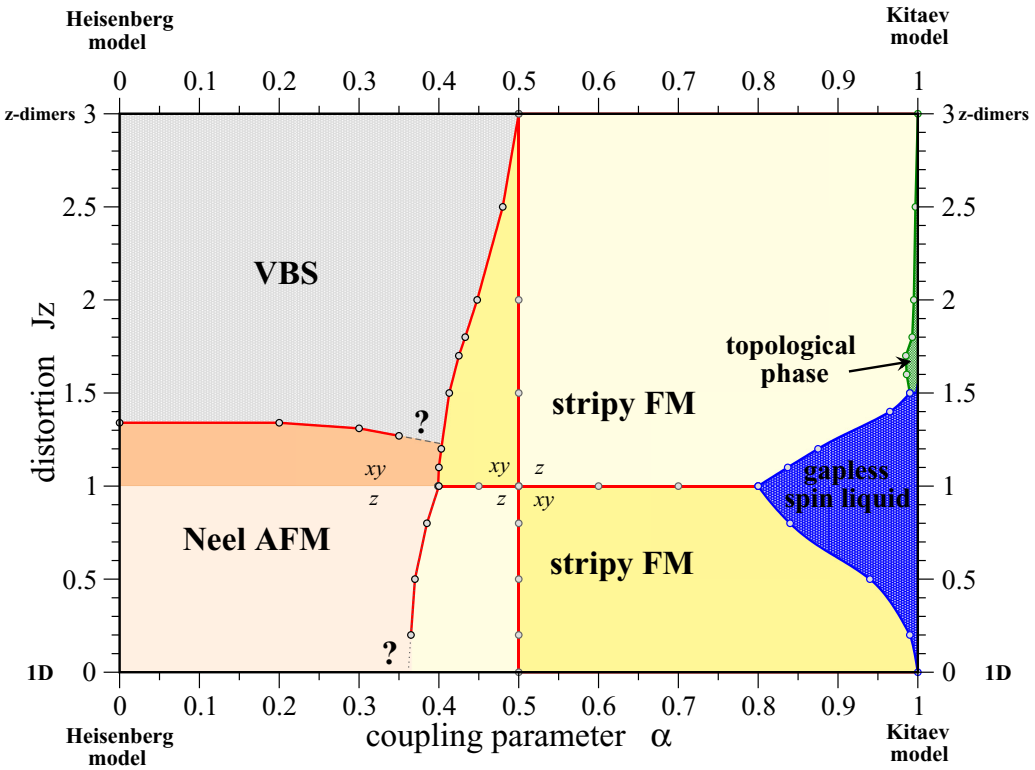

FIG. 11. (Color online) Ground-state phase diagram of the quantum Heisenberg-Kitaev model with regard to the relative strength α of the Heisenberg and Kitaev couplings and the distortion J_z. The line $J_z = 1$ corresponds to the undistorted model, which for increasing coupling parameter α shows a sequence of a Néel ordered antiferromagnet, a stripy-ordered ferromagnet, and a gapless spin liquid around the Kitaev limit. For a finite distortion, the magnetically ordered states undergo a quantum order-by-disorder transition, which locks the spin orientation in the ordered phases to the z (x or y) direction as indicated in the diagram. The quantum phase transitions between these various ordered states are all first-order as indicated by the red solid lines in the phase diagram. For large distortions $J_z \gtrsim 1.35$, the Néel antiferromagnet is destabilized in favor of a valence-bond solid (VBS) state. Arguably, the most interesting phases in this phase diagram are an extended gapless spin liquid around the undistorted Kitaev limit as well as a topologically ordered spin liquid for $J_z > 3/2$ around the Kitaev limit. The possibly continuous phase transitions out of the gapped spin liquid phase is discussed in the main text.

ratio of the Heisenberg and Kitaev couplings, the model can be mapped via the four-sublattice basis transformation illustrated in Fig. 3 to a ferromagnetic Heisenberg model. In fact, such a mapping exists for all values of the distortion J_z, i.e., the quantum model exhibits an entire SU(2) symmetric line for $\alpha = 1/2$. In the four-sublattice rotated basis, the ground state of the quantum model is a simple ferromagnet for $\alpha = 1/2$, which transformed back into the original basis becomes a "stripy ferromagnet" akin to the illustrations in Fig. 4. In the undistorted case ($J_z = 1$), the ground state is sixfold degenerate with the six possible stripy states of Fig. 4 having equal weight in the ground state. This picture changes immediately upon moving away from the $\alpha = 1/2$ line and distorting the exchange couplings. Again, a quantum order-by-disorder transition (detailed in Appendix C) selects a subset of these six stripy states with four different phases emerging around the undistorted ($\alpha = 1/2, J_z = 1$) point in the middle of our phase diagram in Fig. 11. In complete analogy to the classical model, a subset of two stripy FM states locking the spins into the z direction is selected for ($\alpha > 1/2, J_z > 1$) as well as for ($\alpha < 1/2, J_z < 1$). For the other two quadrants ($\alpha < 1/2, J_z > 1$) and ($\alpha > 1/2, J_z < 1$), the opposite subset of four stripy FM states with the spins locking into either the x or y directions are selected by the quantum order-by-disorder mechanism, see Appendix C for details.

Arguably the most interesting phases in our phase diagram are the two spin liquid phases emerging for dominating Kitaev couplings. For the undistorted Heisenberg-Kitaev model, it was previously established [6,14] that the stripy FM phase gives way to a gapless spin liquid phase for $\alpha \approx 0.8$, i.e., Kitaev couplings, which are about eight times larger than the isotropic Heisenberg exchange. This gapless spin liquid phase remains stable when introducing an exchange distortion $J_z \neq 1$ and is found to occupy a rather extended regime in the (α, J_z)-parameter space as illustrated in Fig. 11. For the pure Kitaev model, it is well known [9] that the gapless spin liquid can be gapped out into a topological spin liquid if one introduces an exchange distortion that renders one of the three coupling exchanges dominant, i.e., $J_z \geqslant 3/2$ in our notation, see Fig. 1(c). Upon including a Heisenberg exchange this gapped phase must remain stable for a finite parameter regime—however, since the gap itself is rather small the regime occupied by this topological spin liquid in our (α, J_z)-parameter space reduces to a small sliver as illustrated in Fig. 11. We come back to a more detailed discussion of the emergence of this topological phase as well as the nature of the quantum phase transition out of this phase into the stripy phase in the next section.

Our approach to map out the phase diagram of the quantum Heisenberg-Kitaev model as discussed above is based on various numerical techniques, in particular exact diagonalization (ED) studies and density-matrix renormalization group (DMRG) [35] calculations for small, but highly symmetric clusters with up to $N = 48$ ($N = 24$) sites for the DMRG (ED) calculations, respectively. In order to minimize finite-size effects, we employed periodic boundary conditions and chose the clusters such that they preserve the SU(2) symmetry of the four-sublattice basis transformation introduced in Sec. II A. We used clusters of $N = 24 = 3 \times 4 \times 2$ and $N = 32 = 4 \times 4 \times 2$ sites. For the DMRG calculations, we typically kept

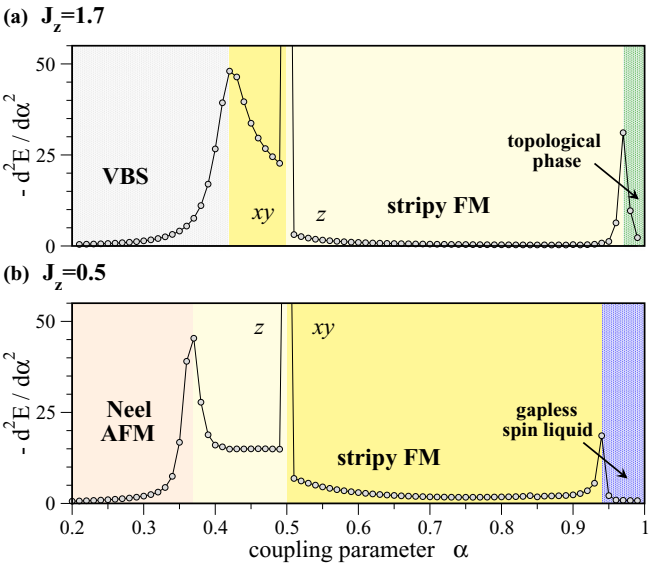

FIG. 12. (Color online) Second derivative of the ground-state energy density as a function of α for two different values of the distortion J_z.

up to $m = 2048$ states in the DMRG block and performed multiple sweeps to converge the observables with the typical truncation error becoming of the order of 5×10^{-6} or smaller. The location of the phase boundaries in the phase diagram (see Fig. 11) are determined by the peak position of the second derivatives of the ground-state energy density, i.e., $d^2E/d\alpha^2$ and d^2E/dJ_z^2. A similar approach has previously been used to successfully map out the phase diagram of the (undistorted) Heisenberg-Kitaev model in a magnetic field [14]. Data for these derivatives along representative cuts in the (α, J_z)-parameter space are shown in Figs. 12 and 13. A

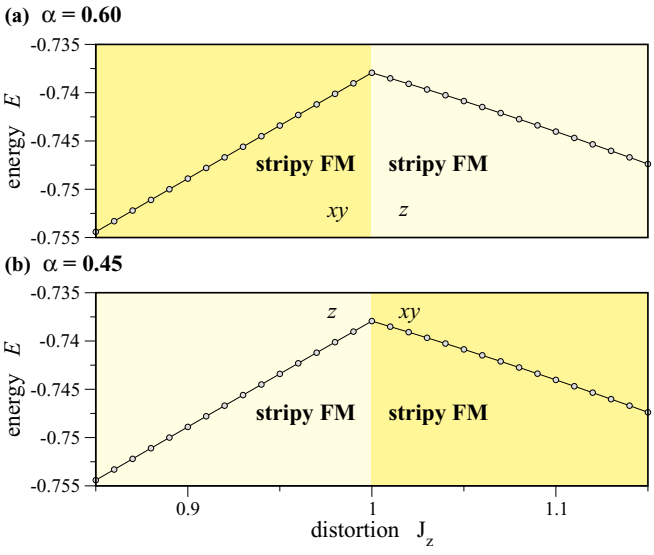

FIG. 13. (Color online) Ground-state energy density as a function of the distortion J_z for two different values of the coupling α. The kink at $J_z = 1$ clearly indicates a first-order transition.

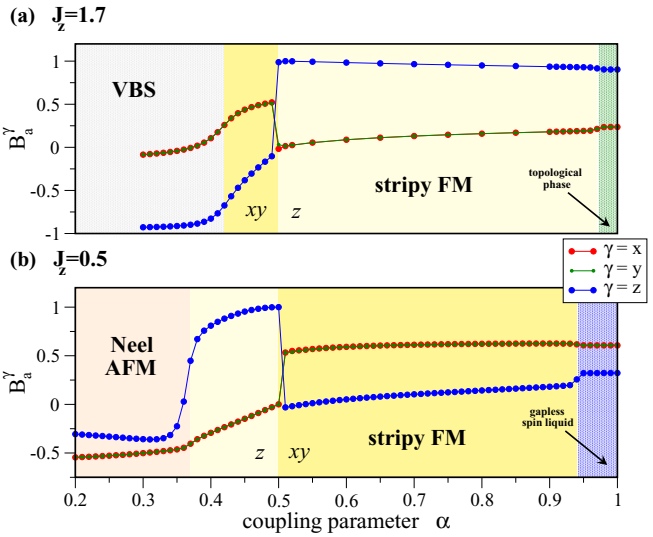

FIG. 14. (Color online) Bond magnetization B_a^γ as a function of α for two different values of the distortion J_z. Here, $\gamma = a = x,y,z$.

very sharp peak in the second derivative—corresponding to a jump of the first derivative of the ground-state energy density, i.e., $\frac{dE}{d\alpha}$ and $\frac{dE}{dJ_z}$—is taken as a signature for a first-order transition and marked by the red solid lines in the phase diagram, while a relative shallow peak in the second derivative data is interpreted as possibly indicating continuous phase transitions.

To further identify the nature of different phases and compare with the classical Heisenberg-Kitaev model, we calculate a "bond magnetization," i.e., the expectation value of the bond operator $B_a^\gamma = \langle S_i^\gamma \cdot S_{i+\hat{a}}^\gamma \rangle$, where $\gamma = x,y,z$ denotes the γ component of spin, and $\hat{a} = \hat{x},\hat{y},\hat{z}$ is the unit vector along an a-bond. As illustrated in Fig. 14, this bond magnetization is a very useful tool to track the quantum order-by-disorder selection in the distorted stripy phases. For example, in the stripy-z phase for $(\alpha > 1/2, J_z > 1)$ and $(\alpha < 1/2, J_z < 1)$, the z-bond magnetization B_z^z is positive since S^z points in the same direction in z bond, while B_x^z and B_y^z are negative because S^z are antiparallel along the x and y bonds (not shown). In addition to the stripy phase, this bond operator can also be used to study the phase transition between different phases, which will increase or decrease rapidly across the phase boundary. As an example, we plot the bond operator B_a^γ with $\gamma = a = x,y,z$ in Fig. 14(b), in which the dotted lines are the phase boundaries determined by B_a^γ, and consistent with the ones determined by the second derivative of the ground-state energy density.

Finally, we want to shortly comment on the quantum order-by-disorder mechanism playing out in the distorted stripy phase. As mentioned earlier, for precisely $\alpha = 1/2$, the system exhibits an additional SU(2) symmetry and its ground state can be characterized by a conventional ferromagnetic order parameter in terms of the four-sublattice transformed $\tilde{S}$ spin variables introduced in Sec. II A. For small deviations from $\alpha = 1/2$, the symmetry of the model is reduced to a discrete one. However, as we saw in Sec. II A when discussing the classical model, one can quickly see that on the mean-field level the actual direction of the ferromagnetic order is not fixed upon introducing a distortion. In fact, as we have shown

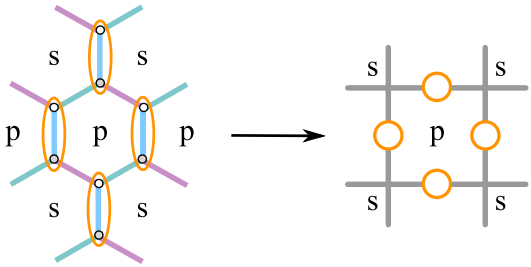

FIG. 15. (Color online) Mapping from the honeycomb lattice to the toric code lattice.

in Sec. II A, thermal fluctuations are ultimately responsible for the eventual ordering along cubic axes in the classical model. An analogous argument applies to the quantum model where quantum fluctuations will favor a locking of the spin orientation along the cubic axes of the model for finite distortions at zero temperature. This effect has been first commented on in Refs. [36] and [6] and is discussed in detail in Appendix C.

B. Phase transition out of the Abelian topological phase

For $J_z = 3$, $J_x = J_y = 0$, the system decouples into z dimers with Hamiltonian H_{ij}^z given in Eq. (2). The Heisenberg term has the singlet state s as the ground state with an excited triplet $\{t^+,t^-,t^0\}$, whereas the Kitaev ferromagnetic term has a degenerate pair of ground states $(t^\pm)$ and a second degenerate pair of excited states (s,t^-). The energies of these states are $E_s/J_z = 5\alpha - 3$, $E_{t^\pm}/J_z = 1 - 3\alpha$, and $E_{t^0}/J_z = 1 + \alpha$. For $\alpha = 1$, one can formulate an effective interaction between the doublet $t^\pm$ degrees of freedom localized on z links and represented by effective spins $\sigma_i^z = \pm 1$. Thus for a given z link, $\sigma_i^z = +1$ for the state $|\uparrow\uparrow\rangle$ and $\sigma_i^z = -1$ for the state $|\downarrow\downarrow\rangle$. Following Kitaev [9], those spins can be located on the links of a square lattice; see Fig. 15. For small J_x, J_y the dimer-dimer interaction can be represented as an effective interaction between the σ's. For the Kitaev model ($\alpha = 1$), the leading interaction is generated at forth order in J_x, J_y, and is a 4-spin interaction equivalent to the toric code model. Explicitly for $J_x = J_y \ll J_z$ [9],

$$H^{(4)} = -J_{\mathrm{TC}} \sum_P Q_P, \tag{31}$$

with $J_{TC} = \frac{J_x^2 J_y^2}{16 J_z^3}$, and the plaquette operator $Q_P = \sigma^y_{\mathrm{left(p)}}\sigma^y_{\mathrm{right(p)}}\sigma^z_{\mathrm{up(p)}}\sigma^z_{\mathrm{down(p)}}$, where P runs over all hexagonal plaquettes of the honeycomb lattice, which become either plaquettes p or stars s on the square lattice of the toric code.

In the presence of the Heisenberg term, we find an interaction already at first order in $J_{x,y}$ that reads simply

$$H^{(1)} = J \sum_{\langle i,j \rangle} \sigma_i^z \sigma_j^z, \tag{32}$$

with $J = J_x(1-\alpha)$. Here, $\langle i,j \rangle$ are nearest neighbors in the square lattice of the toric code. One immediately sees that this term stabilizes a Néel order of the effective spins σ_i^z, which is equivalent to the stripy-z phase in Fig. 4. Therefore the phase transition between the topological phase and stripy phase

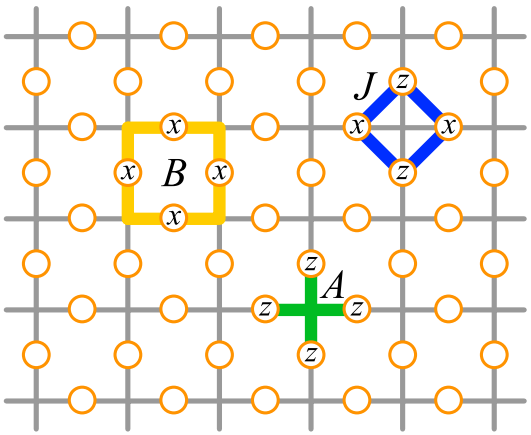

FIG. 16. (Color online) A represents star operators in Eq. (34), B plaquette operators, and J Ising coupling on nearest neighbors.

emanates from the right-top corner of the phase diagram. By comparing the energy scales of the interaction $J_{\rm TC}$, in Eq. (31), stabilizing the topological phase and the Ising interaction J, in Eq. (32), one immediately sees that the transition line approaches the right-top point as

$$1-\alpha \propto (3-J_z)^3. \tag{33}$$

This high power of $(3-J_z)$ is consistent with the very small area occupied by the gapped topological phase in our phase diagram in Fig. 11.

1. *Possibility of condensation of (e,m) excitations*

We propose a simple model to understand the quantum phase transition between the gapped topological phase and stripy phase. This model contains just the two competing interactions that stabilize either phase: the toric code Hamiltonian (31) and the Ising Hamiltonian (32). In order to introduce the standard notation for the toric code model, after permuting the spin indices $(z,x,y)\to(x,y,z)$, and then performing a $-\pi/2$ rotation along y for spins living on vertical bonds in the toric code square lattice defined in Fig. 15, the model becomes

$$H=-A\sum_s\prod_{i\in s}\sigma_i^z-B\sum_p\prod_{i\in p}\sigma_i^x+J\sum_{\langle i,j\rangle}\sigma_i^x\sigma_j^z, \tag{34}$$

where the coupling $J_{\rm TC}$ has been separated into star and plaquette operators with couplings A and B, shown in Fig. 16. In our case $A=B=J_{\rm TC}$. In the last term σ_i^x always belongs to a horizontal bond and σ_j^z to a vertical bond and $\langle i,j\rangle$ are nearest neighbors (see Fig. 16). As a function of J there must be a quantum phase transition between the Z_2 gapped topological phase to the Ising ordered phase at $J\sim J_{\rm TC}$ with spontaneously broken local Ising symmetry:

$$\begin{aligned}\sigma_i^x&\to-\sigma_i^x,\quad i\in\text{horizontal link},\\ \sigma_j^z&\to-\sigma_j^z,\quad j\in\text{vertical link}.\end{aligned} \tag{35}$$

One can write this model in terms of the excitations of the gapped topological phase: (i) electric excitations e living on stars s with -1 eigenvalue of

$$e_s^z=\prod_{i\in s}\sigma_i^z, \tag{36}$$

and (ii) magnetic excitations m living on plaquettes p with -1 eigenvalue of

$$m_p^z=\prod_{i\in p}\sigma_i^x. \tag{37}$$

In the physical Hilbert space, both e and m excitations occur in pairs. Such pairs are created, respectively, by

$$e_{ss'}^x=\prod_{i\in\mathcal{C}_{ss'}}\sigma_i^x,\quad m_{pp'}^x=\prod_{i\in\mathcal{C}_{pp'}}\sigma_i^z, \tag{38}$$

where $\mathcal{C}_{ss'}(\mathcal{C}_{pp'})$ is an arbitrary path along the lattice (dual lattice) connecting stars s,s' (plaquettes p,p') where the two excitations are created. One can check that $\{e_{ss'}^x,e_{s''}^z\}=0$ for $s''=s$ or $s''=s'$, and $[e_{ss'}^x,e_{s''}^z]=0$ otherwise, and the m's satisfy similar relations. Independent of the choice of contours, $e_{ss'}^x$ and $m_{pp'}^x$ commute if the corresponding contours cross an even number of times and anticommute otherwise.

The Hamiltonian is simply

$$\begin{aligned}H(J)=&-A\sum_s e_s^z-B\sum_p m_p^z\\&+J\sum_{\langle i,j\rangle}e_{s_0s_i}^x e_{s_0s_i'}^x m_{p_0p_j}^x m_{p_0p_j'}^x.\end{aligned} \tag{39}$$

Here each horizontal edge i is shared by two stars s_i and s_i' and each vertical edge j shares two plaquettes p_j and p_j'. The reference star s_0 and reference plaquette p_0 are arbitrary and can be thought of as being located at infinity (with open boundary conditions).

Clearly, in the Néel phase, there is a finite expectation value of

$$E=\langle\sigma_i^x\rangle=\langle e_{s_0s_i}^x e_{s_0s_i'}^x\rangle\neq 0 \tag{40}$$

and

$$M=\langle\sigma_j^z\rangle=\langle m_{p_0p_j}^x m_{p_0p_j'}^x\rangle\neq 0, \tag{41}$$

and their relative sign is opposite for $J>0$. In the topological phase, all excitations are gapped and uncorrelated. Thus a natural question is how the e and m excitations condense. Typically, excitations condense at a phase transition as their kinetic energy exceeds the mass gap. From the effective model (39), we see that, to first order in J, individual e and m excitations can not hop thus their excitation energy is $2A$ and $2B$, respectively. On the other hand, their bound state (e,m) does acquire kinetic energy of order J. It can hop along the x direction hence lowering the gap to $2A+2B-2J$. This suggests an interesting type of quantum phase transition consisting of a condensation of the (e,m) bound states for large enough J, which is unusual due to the fermionic nature of those composite particles. It is interesting to explore this possibility on a quantitative level in the future.

C. One-dimensional limit of the Heisenberg-Kitaev model

In the limit of $J_z=0$, corresponding to the bottom in the phase diagram in Fig. 11, the system decomposes into decoupled Heisenberg-Kitaev chains. The physics of such chains has previously been partially explored, in particular with regard to its energy dynamics [37]. Here, we will apply

one-dimensional (1D) field theoretical methods to analytically construct the 1D phase diagram of such Heisenberg-Kitaev chains, and to gain insight into the 2D case by studying the limit of weakly coupled chains.

1. Phase diagram

Our phase diagram of the 1D Heisenberg-Kitaev (HK) model is shown in Fig. 17(a). It contains three exactly solvable points: (i) for $\alpha = 0$, the model is the antiferromagnetic Heisenberg chain, which is described by a conformal field theory (CFT) with central charge $c = 1$. (ii) At $\alpha = 1/2$, the model written in terms of the $\tilde{S}$ spin variables is the ferromagnetic Heisenberg chain, which has dynamical critical exponent $z = 2$. (iii) At $\alpha = 1$, the system is also critical and can be described by a CFT with $c = 1/2$ corresponding to gapless Majorana chains [9]. Below, we describe the phases in between these three exactly solvable points.

It is convenient to express the 1D HK Hamiltonian as the sum of the well studied XXZ model,

$$H_{\mathrm{xxz}}[\Delta] = \sum_i \left(S_i^x S_{i+1}^x + S_i^y S_{i+1}^y + \Delta S_i^z S_{i+1}^z\right), \qquad (42)$$

and a perturbation. Indeed, our model reads

$$\frac{H_{\mathrm{HK}}(S)}{J_x} = (1-2\alpha) H_{\mathrm{xxz}}\left[\frac{1-\alpha}{1-2\alpha}\right] \pm \alpha \delta H, \qquad (43)$$

with

$$\delta H = \sum_i (-1)^{i+1}\left(S_i^x S_{i+1}^x - S_i^y S_{i+1}^y\right). \qquad (44)$$

The $\pm$ signs correspond to alternating chains. The well known phase diagram of the XXZ model is summarized in Fig. 17(b).

We begin by analyzing the small α limit. At $\alpha = 0$, the perturbation to the XXZ chain vanishes and $\Delta = 1$. Our system lies inside the gapless Luttinger liquid phase of the XXZ model, which extends in the range $-1 \leqslant \Delta \leqslant 1$. This phase is described by a Luttinger liquid theory [38], which is characterized by Luttinger parameter K and velocity v, given exactly by

$$K = \frac{\pi}{2(\pi - \arccos\Delta)}, \quad v = \frac{\pi\sqrt{1-\Delta^2}}{2\arccos\Delta}. \qquad (45)$$

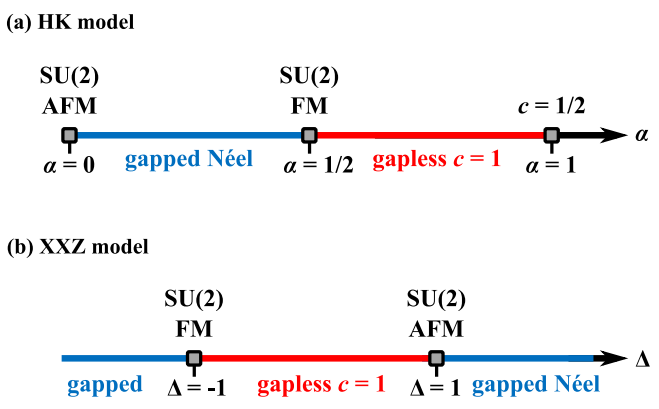

FIG. 17. (Color online) (a) Phase diagram of the 1D Heisenberg Kitaev model. (b) Phase diagram of the XXZ model.

We find that the perturbation to the XXZ model δH has renormalization group scaling dimension

$$x_K = K + K^{-1}. \qquad (46)$$

Hence it is marginal ($x_K = 2$) at $K = 1$ ($\Delta = 0$ in the XXZ model) and, otherwise, it is irrelevant ($x_K > 2$). Since at the vicinity of the point $\alpha = 0$ the perturbation δH is both small and irrelevant, we may safely ignore it. In other words, the HK 1D model at $\alpha = 0^+$ and the XXZ model at $\Delta = 1^+$ differ only by the irrelevant operator δH. When α becomes nonzero and positive, Δ increases above unity in the XXZ chain, and then the gapless phase is destroyed and the chain undergoes a Kosterlitz Thouless transition into a Néel ordered state along z. For the field theoretical description of this transition in the XXZ model we refer the reader to Ref. [38] and references therein.

Translating the Néel order to the $\tilde{S}$ variables, one obtains the ferromagnetic-z phase, e.g., $\uparrow\uparrow\uparrow\uparrow$. This order parameter coincides with that of the ferromagnetic point at $\alpha = 1/2$. Therefore we expect that the Néel ordered phase (in terms of the original spin variables) persists in the entire range $0 < \alpha \leqslant 1/2$.

We now analyze the vicinity of the point $\alpha = 1/2$. It is convenient to write the HK model in terms of the $\tilde{S}$ spin variables using Eq. (3). After a π rotation around the z axis of each second spin, one can rearrange terms into a sum of an XXZ model and a perturbation,

$$\frac{H_{\mathrm{HK}}(\tilde{S})}{J_x} = \alpha H_{\mathrm{xxz}}\left[\frac{\alpha-1}{\alpha}\right] \pm (2\alpha - 1)\delta H. \qquad (47)$$

We see that $\alpha = 1/2$ brings us to the point $\Delta = -1$ in the XXZ model. This point is connected to the gapless phase of the XXZ model, although it has different universality with vanishing velocity, see Eq. (45), and dynamical critical exponent $z = 2$.

We now consider α slightly larger than $1/2$. Since the perturbation to the XXZ model in terms of the $\tilde{S}$ spins, δH, has exactly the same form as the perturbation in terms of original spins, S, we draw the same conclusion regarding the irrelevance of δH. We have again a model that up to an irrelevant operator is equivalent to the XXZ model. We see that moving to the right from $\alpha = 1/2$ is equivalent to moving to the right from $\Delta = -1$ in the XXZ model, entering into the gapless Luttinger liquid phase. We expect that the end point of the Luttinger liquid phase is the 1D limit of the Kitaev Z_2 liquid, $\alpha = 1$. This spin liquid does not have any continuous symmetry. This is consistent with the statement that only upon approaching the point $\alpha = 1$ the operator δH becomes relevant. Using the scaling dimension of δH, Eq. (46), this implies for the Luttinger liquid parameter $K \to 1$ upon approaching the Kitaev limit. Thus the region $1/2 < \alpha < 1$ maps to the region $-1 < \Delta < 0$ in the XXZ model.

The existence of a gapped phase for $0 < \alpha < 1/2$ as well as the persistence of a $c = 1$ gapless phase in the parameter regime $1/2 < \alpha < 1$ is nicely confirmed by DMRG simulations of chains with open and periodic boundary conditions with up to $L = 256$ sites, see Fig. 18. For the extended gapless phase, the central charge of the conformal field theory describing the gapless system can easily be extracted by fitting

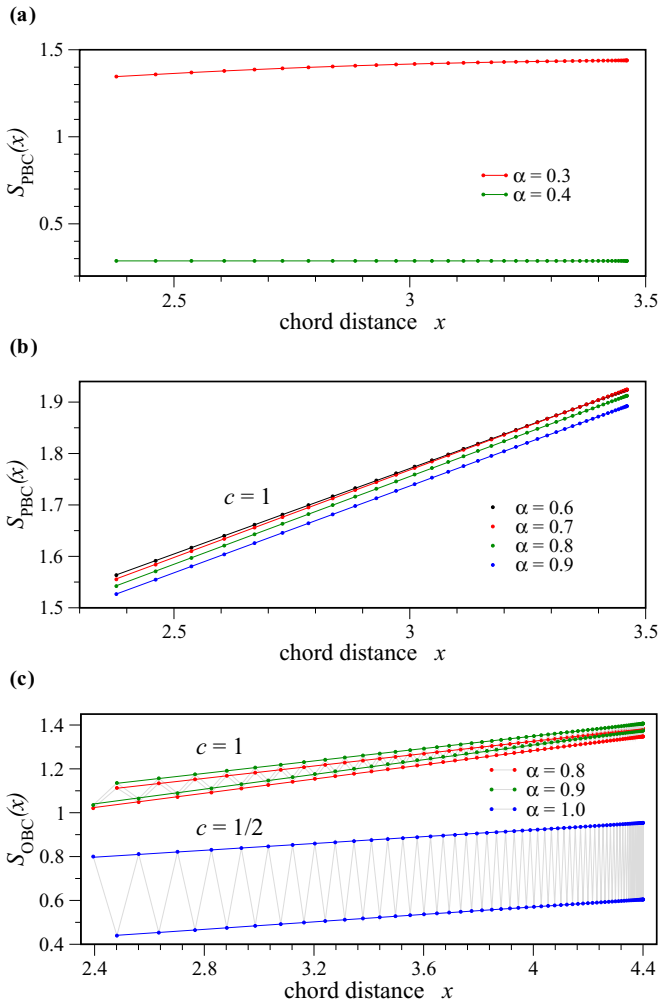

FIG. 18. (Color online) Entanglement scaling for the 1D Heisenberg-Kitaev chain for various coupling strength α. (a) Data for a periodic $L = 100$ site chain in the gapped phase for $\alpha < 1/2$. (b) Data for a periodic $L = 100$ site chain in the gapless phase for $\alpha > 1/2$. (c) Data for an open $L = 256$ site chain in the gapless phase for $\alpha > 1/2$ and $\alpha = 1$. Boundary effects of the open chain result in an odd-even staggering.

the entanglement entropy to the analytical form

$$S(x) = \frac{c}{3\eta}\, x + O(1)\,, \tag{48}$$

where $x = \ln[\frac{\eta L}{\pi} \sin(\frac{\pi l}{L})]$ is the logarithm of the so-called chord distance for a cut dividing the chain into segments of length l and $L - l$ and periodic (open) boundary conditions are indicated by the parameter $\eta = 1$ or 2, respectively. Performing such a fit as indicated by the solid lines in Fig. 18 nicely confirms the expected central charge of $c = 1$. In the Kitaev limit $\alpha = 1$, the gapless phase is verified to be described by $c = 1/2$ conformal field theory, as validated by our numerical simulations [39] shown in Fig. 18(c).

2. *Insight about 2D*

Having constructed the phase diagram of the 1D HK model at $J_z = 0$, we now consider perturbatively the coupling between the chains by studying the effect of a small J_z. This will be useful for the purpose of locating the precise position of the phase transition between the Néel and stripy phase when $J_z \to 0$, which will be the focus of this section.

In terms of the original spins, the interchain Hamiltonian is

$$\begin{aligned} H_\perp = H_z &= \sum_{\text{z-links}} J_z\big[(1-\alpha)\mathbf{S}_i\mathbf{S}_j - (2\alpha)S_i^z S_j^z\big] \\ &= \sum_{\text{z-links}} J_z\big[(1-\alpha)2(S_i^+ S_j^- + S_i^- S_j^+) \\ &\quad + (1-3\alpha)S_i^z S_j^z\big]. \end{aligned} \tag{49}$$

For $0 < \alpha < 1/2$, the chains are ordered and gapped already on the 1D level characterized by the Néel order parameter $M(j)$. On the level of expectation values, we have $\langle S_{i,j}^z\rangle = (-1)^i M(j)$ where j labels different chains. Here, the notation $S_{i,j}^z$ refers to a deformation of the honeycomb into a brickwall lattice. Within this ordered state, the interchain coupling acts classically and couples $M(j)$ to $M(j \pm 1)$. We thus obtain two regimes for the 2D system.

(i) $0 < \alpha < 1/3$. In this regime, the effective interchain coupling is antiferromagnetic, leading to $M(j) = -M(j \pm 1)$. This phase is the 2D Néel antiferromagnet. The order parameter is $\sum_{i,j}(-1)^{i+j}\langle S_{i,j}^z\rangle$.

(ii) $1/3 < \alpha < 1/2$. In this regime, the effective interchain coupling is ferromagnetic leading to $M(j) = M(j \pm 1)$. This phase is the stripy z phase. The order parameter is $\sum_{i,j}(-1)^i\langle S_{i,j}^z\rangle = \sum_{i,j}\langle \tilde{S}_{i,j}^z\rangle$ corresponding to ferromagnetic order of the rotated spin variables.

Thus using weak chain coupling in the regime $\alpha < 1/2$, we found the Néel antiferromagnet as well as the stripy phase, which exist at strong interchain coupling $J_z = 1$. It is therefore reasonable that the phases we found from the 1D limit are indeed connected to those found earlier along the C_3 symmetric line without phase transitions in between. This is, indeed, confirmed by our numerical calculation, see Fig. 11. It is interesting that the transition between the Néel AF and stripy-z phases along the 1D line occurs exactly at $\alpha = 1/3$ as for the classical model (see Fig. 2). The discrepancy with the numerical transition point at $J_z = 0$ between the Néel AF and stripy phase could result from a finite-size effect.

IV. SUMMARY

To summarize, we have used a combination of numerical and analytical methods to establish the rich phase diagram for the distorted Heisenberg-Kitaev model considering both the classical and quantum version of the model. The effect of a finite distortion on the magnetically ordered phases of the undistorted model is an order-by-disorder driven transition, which locks the spin orientation in the ordered phases to the z (x or y) directions—the precise form of the locking is found to be sensitive to both the strength of the distortion as well as the relative coupling strength of the Heisenberg and Kitaev-type interactions.

The physics around the Kitaev limit proves most interesting in both the classical and quantum versions of the model. For the classical model, we have discussed the emergence of a classical spin liquid with a Coulomb gas description in

the undistorted Kitaev limit and its modifications for finite distortions. For the quantum model, the well-known gapless spin liquid around the undistorted Kitaev limit turns out to be remarkably stable also in the presence of substantial distortions. This behavior should be contrasted to the gapped topological spin liquid that arises for strong distortions in the Kitaev limit. The effect of an additional Heisenberg exchange is found to quickly destabilize this phase.

With regard to future work a deeper understanding of the precise nature of these phase transition between the topological and nontopological phases in this phase diagram is probably most desirable. Various recent studies [40–47] have addressed the phase transitions between the gapped Z_2 topological phase of Kitaev's toric code model and conventionally ordered states. Some of these transitions are well-understood continuous phase transitions arising from the condensation of one of the elementary (bosonic) excitations of the toric code, often referred to as electric charges (e) or magnetic vortices (m), as it is the case for the phase transition induced by a single-component magnetic field pointing along one of the two longitudinal directions. Our analysis of the distorted Heisenberg-Kitaev model has led to an effective model, which potentially paves the path to a different type of phase transition arising from the simultaneous condensation of the fermionic (em) bound state of an electric and magnetic excitation, which drives the system from the Z_2 topological phase to a conventional phase with stripy order. Such fermionic (em) bound states have been previously discussed in the context of the single and two-component (longitudinal) magnetic field transitions [41,42,44], transverse field transitions [43], and in more general field theoretical terms [48]. Similarly, the nature of the phase transition between the stripy phase and the gapless topological phase, which has been a topic of recent interest [6,14–16], may be further explored in our distorted model where one can benefit from anisotropic limits.

ACKNOWLEDGMENTS

We thank L. Balents, P. Fendley, N. Perkins, A. Rosch, and K. P. Schmidt for insightful discussions. We also thank O. Wohak for his contributions to the early stages of the simulations of the classical models. E.S. was supported by the A.V. Humboldt Foundation and an ISF grant. H.C.J. was supported by the Templeton Fund. S.T. acknowledges hospitality of the Aspen Center for Physics and partial support from DFG SFB TR12. The numerical simulations were performed in part on the CHEOPS cluster at RRZK Cologne. We further acknowledge computing support from the Center for Scientific Computing at the CNSI and MRL supported through NSF grants NSF MRSEC (DMR-1121053) and NSF CNS-0960316, respectively.

APPENDIX A: CLASSICAL ORDER BY DISORDER MECHANISM

We now provide the details of the derivation of the effective Hamiltonian Eq. (13) starting from the continuum model Eq. (8). This effective Hamiltonian of $\hat{\mathbf{e}}$ is defined via integrating over the fluctuations π_a (defined in Eq. (10),

$$e^{-H_{\rm eff}[\hat{\mathbf{e}}]/T} = \int \mathcal{D}\pi_a(\mathbf{r}) e^{-\mathcal{H}[\hat{\mathbf{e}},\pi_a(\mathbf{r})]/T}. \tag{A1}$$

We now compute this effective Hamiltonian explicitly by expanding $\mathcal{H}[\hat{\mathbf{e}},\pi_a(\mathbf{r})]$ up to quadratic order in the fluctuations $\pi_a(\mathbf{r})$. $\mathcal{H}[\hat{\mathbf{e}},\pi_a(\mathbf{r})]$ contains a Heisenberg part and a Kitaev part. For the Heisenberg part, we use

$$(\nabla_{\mathbf{u}_\gamma}\mathbf{M})^2 = (\nabla_{\mathbf{u}_\gamma}\pi_1)^2 + (\nabla_{\mathbf{u}_\gamma}\pi_2)^2 + \mathcal{O}\big(\pi_a^4\big), \tag{A2}$$

which does not depend on the magnetization direction $\hat{\mathbf{e}}$. For the Kitaev term, we have

$$\nabla_{\mathbf{u}_\gamma} M^\gamma = \hat{e}_1^\gamma \nabla_{\mathbf{u}_\gamma}\pi_1 + \hat{e}_2^\gamma \nabla_{\mathbf{u}_\gamma}\pi_2 + \mathcal{O}(\pi^2), \tag{A3}$$

which depends on the magnetization direction $\hat{\mathbf{e}}$ through its complementary orthogonal vectors $\hat{\mathbf{e}}_1$ and $\hat{\mathbf{e}}_2$. In k space,

$$\mathcal{H}[\hat{\mathbf{e}},\pi_a(\mathbf{r})] = \frac{\mathcal{J}}{2}\sum_{\mathbf{k}}\sum_{a,b}\pi_a(\mathbf{k})h_{ab}(\mathbf{k})\pi_b(-\mathbf{k}), \tag{A4}$$

with $\mathcal{J} = J/A_{\rm hex}$ and

$$h_{ab}(\mathbf{k}) = \sum_\gamma \big[((1-\alpha)\delta_{ab} + (4\alpha-2)e_a^\gamma e_b^\gamma\big]k_{u_\gamma}^2, \tag{A5}$$

where $k_{u_\gamma} = \mathbf{k}\cdot\hat{\mathbf{u}}_\gamma$. Performing the Gaussian integrals over $\pi_a(\mathbf{k})$, we arrive at the effective Hamiltonian

$$\frac{H_{\rm eff}}{T} = \sum_{\mathbf{k}} \ln\det\left(\frac{\mathcal{J}}{2T}\hat{h}(\mathbf{k})\right), \tag{A6}$$

where $\det\hat{h} = h_{11}h_{22} - h_{12}h_{21}$. In order to proceed analytically we assume that the anisotropic Kitaev term is small, $|\alpha - 1/2| \ll 1$. Then, up to a constant, we can expand

$$\frac{H_{\rm eff}}{T} = \sum_{\mathbf{k}} \ln\det\left(\delta_{ab} + \epsilon\sum_\gamma e_a^\gamma e_b^\gamma \frac{k_{u_\gamma}^2}{|k|^2}\right). \tag{A7}$$

with small parameter $\epsilon = \frac{4}{3}\frac{2\alpha-1}{1-\alpha} \propto (2\alpha-1)$.

We further make the simplifying approximation of a circular Brillouin zone of radius k_{BZ} such that the total number of sites is $N = \sum_{\mathbf{k}} = \mathcal{A}\int_{|\mathbf{k}|<k_{BZ}}\frac{d^2k}{(2\pi)^2}$ with total area $\mathcal{A} = NA_{\rm hex}$. Using polar coordinates for the momentum integral and performing the integral over $|\mathbf{k}|$, we obtain $\frac{H_{\rm eff}}{NT} = \int_0^{2\pi}\frac{d\theta}{2\pi}\ln\mathrm{tr}(\mathbf{1}+\epsilon\hat{A})$. Next, we use the identity $\ln\det = \mathrm{tr}\ln$ and expand the ln up to quadratic order in $\alpha - 1/2$, to obtain

$$\frac{H_{\rm eff}}{NT} = \int_0^{2\pi}\frac{d\theta}{2\pi}\left[\epsilon\,\mathrm{tr}(\hat{A}) - \frac{1}{2}\epsilon^2\,\mathrm{tr}(A^2)\right] + \mathcal{O}\left(\alpha-\frac{1}{2}\right)^3, \tag{A8}$$

with $A_{ab} = \sum_\gamma e_a^\gamma e_b^\gamma \cos^2(\theta-\theta_\gamma)$, $\theta_x = 2\pi/3$, $\theta_y = 4\pi/3$, $\theta_z = 0$. Using $\int_0^{2\pi}\frac{d\theta}{2\pi}\cos^2(\theta-\theta_\gamma) = 1/2, (\gamma = x,y,z)$, we have simply for the first order term $\int_0^{2\pi}\frac{d\theta}{2\pi}\mathrm{tr}\,A = \frac{1}{2}\mathrm{tr}\sum_\gamma e_a^\gamma e_b^\gamma = \frac{1}{2}(\hat{\mathbf{e}}_1^2 + \hat{\mathbf{e}}_2^2) = 1$ which is a constant independent of $\hat{\mathbf{e}}$. The second-order term is evaluated similarly. Using $\int_0^{2\pi}\frac{d\theta}{2\pi}\cos^2(\theta-\theta_\gamma)\cos^2(\theta-\theta_{\gamma'}) = \frac{3}{16}(1+\delta_{\gamma\gamma'})$, we have

$$\frac{H_{\rm eff}}{NT} = -\frac{2}{3}(2\alpha-1)^2\sum_{\gamma,\gamma'}\sum_{a,b=1,2} e_a^\gamma e_b^\gamma e_b^{\gamma'} e_a^{\gamma'}(1+\delta_{\gamma\gamma'}). \tag{A9}$$

As the unit vectors $\hat{\mathbf{e}}_1, \hat{\mathbf{e}}_2, \hat{\mathbf{e}}$ form an orthonormal basis, one can readily derive the identities $\sum_{\gamma,\gamma'}\sum_{a,b=1,2} e_a^\gamma e_b^\gamma e_b^{\gamma'} e_a^{\gamma'} =$

2, and

$$\sum_{\gamma}\sum_{a,b=1,2} e_a^{\gamma} e_b^{\gamma} e_b^{\gamma} e_a^{\gamma} = \sum_{\gamma} (\hat{e}^{\gamma})^4 + \text{const.} \quad \text{(A10)}$$

As a result, we obtain the decisive term in the effective Hamiltonian, up to a constant and up to quadratic order in $2\alpha - 1$,

$$\frac{H_{\text{eff}}}{NT} = -\frac{2}{3}(2\alpha-1)^2\left[(\hat{e}^x)^4 + (\hat{e}^y)^4 + (\hat{e}^z)^4\right]. \quad \text{(A11)}$$

APPENDIX B: EMERGENT MAGNETOSTATICS IN THE CLASSICAL KITAEV MODEL

The aim of this section is to provide a brief, self-consistent description of the Coulomb gas formulation of the spin liquid state in the undistorted classical Kitaev model, i.e., we consider the situation of $J_x = J_y = J_z = J$ only. Given an arbitrary configuration of spins S^{γ}, we can assign to each lattice bond $(\mathbf{R}_i, \gamma)$ connecting sublattice a site (filled circles in Fig. 8) $\mathbf{R}_i$ to a neighboring sublattice b (empty circles in Fig. 8) site $\mathbf{R}_i + \hat{\mathbf{u}}_{\gamma}$, a vector $\mathbf{E} = E(\mathbf{R}_i;\gamma)\hat{\mathbf{u}}_{\gamma}$, with

$$E(\mathbf{R}_i;\gamma) = \left(S^{\gamma}_{a,\mathbf{R}_i}\right)^2 - \tfrac{1}{3}. \quad \text{(B1)}$$

The discrete divergence of the $\mathbf{E}$-field at vertices $\mathbf{R}_i$ of sublattice a vanishes by definition, $\sum_{\gamma} E(\mathbf{R}_i;\gamma) = 0$, since $|\mathbf{S}_{\mathbf{R}_i}| = 1$. The nontrivial property of the ground states of the classical Kitaev model is that they satisfy a divergence-free condition also in the b sublattice,

$$\text{vertex } \mathbf{R}_i + \hat{\mathbf{u}}_z: \quad \nabla\cdot\mathbf{E} = \sum_{\gamma} E(\mathbf{R}_i - \mathbf{r}_{\gamma};\gamma) = 0, \quad \text{(B2)}$$

where $\mathbf{r}_{\gamma} = \hat{\mathbf{u}}_z - \hat{\mathbf{u}}_{\gamma}$. This condition follows from the formation of dimer-covering states; see Fig. 8. In such states, for every spin on sublattice a, there exists a neighboring spin in sublattice b such that both spins point ferromagnetically along the direction of the connecting bond.

It is not difficult to show that the dimer covering states have the lowest possible energy for the classical Kitaev model [17]. The partition function

$$Z = \int \prod_{\mathbf{R}_i} \frac{dS_{a,\mathbf{R}_i}}{4\pi}\frac{dS_{b,\mathbf{R}_i}}{4\pi} e^{-H/T} \quad \text{(B3)}$$

can be evaluated by writing the Hamiltonian as $H = -\sum_{\mathbf{R}_i} \mathbf{S}_{a,\mathbf{R}_i}\mathbf{B}_{\mathbf{R}_i}$, where $\mathbf{B}_{\mathbf{R}_i} = \sum_{\gamma} J_{\gamma} S^{\gamma}_{b,\mathbf{R}_i+\hat{\mathbf{u}}_{\gamma}}\hat{\mathbf{u}}_{\gamma}$, and then performing the integral over spins of sublattice a which appear to be free except for an external field $\mathbf{B}_{\mathbf{R}_i}$. This gives

$$Z = \int \prod_{\mathbf{R}_i} \frac{dS_{b,\mathbf{R}_i}}{4\pi} e^{-\sum_{\mathbf{R}_i} h_{\text{eff}}(|\mathbf{B}_{\mathbf{R}_i}|)/T}. \quad \text{(B4)}$$

Now, using the convexity of the effective Hamiltonian $h_{\text{eff}}(B) = -T\ln\frac{T\sinh(B/T)}{B}$, which implies $\langle h_{\text{eff}}(x)\rangle < h_{\text{eff}}(\langle x\rangle)$, one sees that the total energy is minimized when all $|\mathbf{B}_{\mathbf{R}_i}|$'s are equal. As $\sum_{\mathbf{R}_i}|\mathbf{B}_{\mathbf{R}_i}| = NJ$ the minimum occurs when $|\mathbf{B}_{\mathbf{R}_i}| = J$. This situation is indeed achieved in the dimer-covering state. It should be noted that there exist an additional continuous slide degree of freedom within the ground state [34].

The emergent divergence-free $\mathbf{E}$-field leads to peculiar features in observables that depend on $\mathbf{E}$. For example, consider the bond-energy correlation $\langle (S_i^z)^2 (S_j^z)^2\rangle - 1/9$, which measures the $\langle E^z E^z\rangle$ correlation. The following simple derivation applies to Coulomb phases in general, so we now coarse grain the original lattice and consider separations $|i-j|$ much larger than the lattice spacing. For such a long distance description, we can think of $\mathbf{E}$ as a field on a continuous space that satisfies the divergence free condition

$$\nabla\cdot\mathbf{E}(\mathbf{r}) = 0. \quad \text{(B5)}$$

At zero temperature, all divergence free field configurations are equally likely. At finite temperature (low enough to avoid considerable charge density), field configurations having locally a net polarization are suppressed entropically, leading to the leading quadratic term in the effective free energy:

$$F = \frac{\mathcal{K}}{2}\int d^d r [\mathbf{E}(\mathbf{r})]^2. \quad \text{(B6)}$$

Here, the constant $\mathcal{K}$ is analogous to the permittivity in electrodynamics and this coarse grain formulation may be considered in arbitrary dimension d. The divergence-free constraint Eq. (B5) is easily taken into account in momentum space where it reads

$$\mathbf{k}\cdot\mathbf{E}(\mathbf{k}) = 0, \quad \text{(B7)}$$

and the free energy is $F = \frac{\mathcal{K}}{2}\sum_{\mathbf{k}} |E^{\perp}(\mathbf{k})|^2$. Here, $E^{\perp}(\mathbf{k})$ refers to the components (single component in 2D) of $\mathbf{E}$ perpendicular to $\mathbf{k}$. The correlation function is calculated directly from the equipartition $\langle E^{\mu}(-\mathbf{k})E^{\nu}(\mathbf{k}')\rangle = \mathcal{K}^{-1}P_{\mu\nu}\delta_{\mathbf{k},\mathbf{k}'}$, where in a basis whose first element is parallel to $\mathbf{k}$ we have $P = \left(\begin{smallmatrix} 0 & 0 \\ 0 & \mathbf{1}_{d-1}\end{smallmatrix}\right)$. Writing the projector P in a general basis gives

$$\langle E^{\mu}(-\mathbf{k})E^{\nu}(\mathbf{k}')\rangle = \mathcal{K}^{-1}\left(\delta_{\mu\nu} - \frac{k_{\mu}k_{\nu}}{|\mathbf{k}|^2}\right)\delta_{\mathbf{k},\mathbf{k}'}. \quad \text{(B8)}$$

This implies a power-law decay of correlation functions in real space $\langle E^{\mu}(-\mathbf{k})E^{\nu}(\mathbf{k}')\rangle \propto \frac{1}{|\mathbf{r}|^d}$. This general result implies pinch points in correlation functions, since the correlation functions depend on how the limit $|\mathbf{k}| \to 0$ is approached. For our model, this implies for the $(S_i^z)^2$ correlation the form

$$S(\mathbf{k}) = \left\langle \left(S_i^z\right)^2 \left(S_j^z\right)^2\right\rangle_{\mathbf{k}} \propto \frac{k_y^2}{k_x^2 + k_y^2}, \quad \text{(B9)}$$

leading to the pinch point at $|\mathbf{k}| = 0$.

APPENDIX C: QUANTUM ORDER-BY-DISORDER MECHANISM

Following a similar logic as in the classical case, here we will determine the magnetization direction of the quantum stripy phase, by following an order-by-disorder calculation of the fluctuations. Technically, the quantum fluctuations will be taken into account by a large-S expansion of the $\tilde{S}$ spin variables, with Hamiltonian (3). We represent the spins in sublattice a and b using Holstein-Primakoff bosons a_{R_i} and b_{R_i}, respectively, as

$$\tilde{\mathbf{S}}_{a,R_i} = (S - a^{\dagger}_{R_i}a_{R_i})\hat{\mathbf{e}} + \sqrt{\frac{S}{2}}\left[\hat{\mathbf{e}}_1\left(a_{R_i} + a^{\dagger}_{R_i}\right) - i\hat{\mathbf{e}}_2\left(a_{R_i} - a^{\dagger}_{R_i}\right)\right],$$

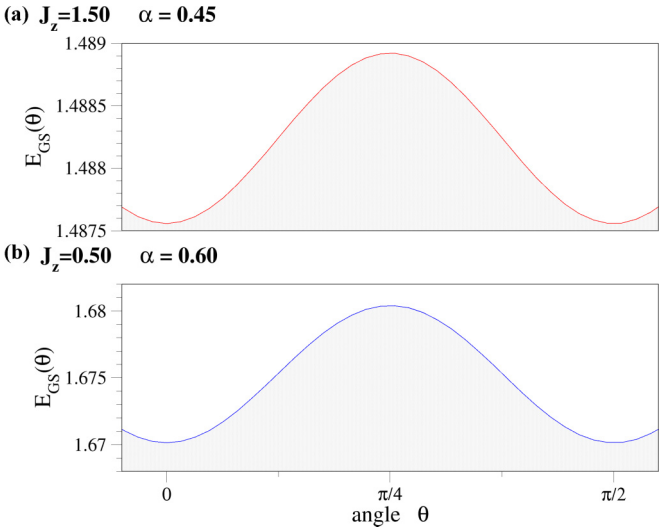

FIG. 19. (Color online) Quantum fluctuation contribution to the ground-state energy per unit cell as a function of azimuthal angle along the equator as parameterizing the magnetization $\hat{\mathbf{e}}$, with $\alpha = 0.45$ $J_z = 1.5$, or alternatively for $\alpha = 0.6$ $J_z = 0.5$ showing minima along cubic axes. Numerical evaluation of the k sum in Eq. (C6) has been done for a honeycomb lattice with 10×10 unit cells with periodic boundary conditions.

$$\tilde{\mathbf{S}}_{b,R_i} = \big(S - b^\dagger_{R_i} b_{R_i}\big)\hat{\mathbf{e}} + \sqrt{\frac{S}{2}}\big[\hat{\mathbf{e}}_1\big(b_{R_i} + b^\dagger_{R_i}\big) - i\hat{\mathbf{e}}_2\big(b_{R_i} - b^\dagger_{R_i}\big)\big]. \quad \text{(C1)}$$

We have expanded around a uniform ground state with magnetization direction $\hat{\mathbf{e}}_1 \times \hat{\mathbf{e}}_2 = \hat{\mathbf{e}}$. The terms in the Hamiltonian of order S^2 give the classical energy. At this level, the energy is independent on the magnetization direction $\hat{\mathbf{e}}$. We now evaluate the next leading order terms in a $1/S$ expansion. It is convenient to compute the spin-spin couplings appearing in the Hamiltonian. For the Heisenberg, we have the simple form

$$\tilde{\mathbf{S}}_a \cdot \tilde{\mathbf{S}}_b = -S(a^\dagger a + b^\dagger b - a^\dagger b - a b^\dagger). \quad \text{(C2)}$$

For the Kitaev term, we have

$$\tilde{\mathbf{S}}^\gamma_a \tilde{\mathbf{S}}^\gamma_b = \left((S - a^\dagger a)\hat{\mathbf{e}}^\gamma + \sqrt{\frac{S}{2}}\big[\hat{\mathbf{e}}^\gamma_1(a + a^\dagger) - i\hat{\mathbf{e}}^\gamma_2(a - a^\dagger)\big]\right) \times \left((S - b^\dagger b)\hat{\mathbf{e}}^\gamma + \sqrt{\frac{S}{2}}\big[\hat{\mathbf{e}}^\gamma_1(b + b^\dagger) - i\hat{\mathbf{e}}^\gamma_2(b - b^\dagger)\big]\right). \quad \text{(C3)}$$

This includes an $\mathcal{O}(S^{3/2})$ term linear in the bosons $a, a^\dagger, b$, and $b^\dagger$. This linear term contains one contribution proportional to $\hat{\mathbf{e}}^\gamma \hat{\mathbf{e}}^\gamma_1$, and another proportional to $\hat{\mathbf{e}}^\gamma \hat{\mathbf{e}}^\gamma_2$. Upon summing over the three links connected to either a or b these contributions vanish since $\hat{\mathbf{e}} \cdot \hat{\mathbf{e}}_1 = \hat{\mathbf{e}} \cdot \hat{\mathbf{e}}_2 = 0$.

The $\mathcal{O}(S)$ term is quadratic in the bosonic operators. After Fourier transformation, the $\mathcal{O}(S)$ term can be written as

$$\frac{\tilde{H}}{S} = \sum_k \left[\Psi^\dagger_k \hat{h}_k \Psi_k + (2 - 4\alpha)\sum_\gamma J_\gamma (\hat{\mathbf{e}}^\gamma)^2\right], \quad \Psi_k = (a_k \quad b_k \quad a^\dagger_{-k} \quad b^\dagger_{-k})^T \quad \text{(C4)}$$

with

$$\hat{h}_k = \sum_\gamma J_\gamma \left[\frac{\alpha - 1}{2}\begin{pmatrix} -1 & e^{i\mathbf{k}\cdot r_\gamma} & 0 & 0 \\ e^{-i\mathbf{k}\cdot r_\gamma} & -1 & 0 & 0 \\ 0 & 0 & -1 & e^{i\mathbf{k}\cdot r_\gamma} \\ 0 & 0 & e^{-i\mathbf{k}\cdot r_\gamma} & -1 \end{pmatrix} + \frac{1 - 2\alpha}{2}\begin{pmatrix} -2(\hat{\mathbf{e}}^\gamma)^2 & \big((\hat{\mathbf{e}}^\gamma_1)^2 + (\hat{\mathbf{e}}^\gamma_2)^2\big)e^{i\mathbf{k}\cdot r_\gamma} & 0 & \big(\hat{\mathbf{e}}^\gamma_1 + i\hat{\mathbf{e}}^\gamma_2\big)^2 e^{i\mathbf{k}\cdot r_\gamma} \\ \big((\hat{\mathbf{e}}^\gamma_1)^2 + (\hat{\mathbf{e}}^\gamma_2)^2\big)e^{-i\mathbf{k}\cdot r_\gamma} & -2(\hat{\mathbf{e}}^\gamma)^2 & \big(\hat{\mathbf{e}}^\gamma_1 + i\hat{\mathbf{e}}^\gamma_2\big)^2 e^{-i\mathbf{k}\cdot r_\gamma} & 0 \\ 0 & \big(\hat{\mathbf{e}}^\gamma_1 - i\hat{\mathbf{e}}^\gamma_2\big)^2 e^{i\mathbf{k}\cdot r_\gamma} & -2(\hat{\mathbf{e}}^\gamma)^2 & \big((\hat{\mathbf{e}}^\gamma_1)^2 + (\hat{\mathbf{e}}^\gamma_2)^2\big)e^{i\mathbf{k}\cdot r_\gamma} \\ \big(\hat{\mathbf{e}}^\gamma_1 - i\hat{\mathbf{e}}^\gamma_2\big)^2 e^{-i\mathbf{k}\cdot r_\gamma} & 0 & \big((\hat{\mathbf{e}}^\gamma_1)^2 + (\hat{\mathbf{e}}^\gamma_2)^2\big)e^{-i\mathbf{k}\cdot r_\gamma} & -2(\hat{\mathbf{e}}^\gamma)^2 \end{pmatrix}\right].$$

The second term in Eq. (C4) is proportional to the classical term $\propto S^2$. Hence it does not lift the degeneracy of the ground-state manifold. Ignoring this term, after Bogoliubov transformation [49], the quadratic Hamiltonian becomes

$$\sum_k \sum_{\mu=1}^{2} \omega_{k,\mu}(\Gamma^\dagger_{k\mu}\Gamma_{k\mu} + \Gamma_{k\mu}\Gamma^\dagger_{k\mu}), \quad \text{(C5)}$$

where $\omega_{k,\mu} > 0$ $(\mu = 1,2)$, and $(\omega_{k,1}, \omega_{k,2}, -\omega_{k,1}, -\omega_{k,2})$ are the eigenvalues of the matrix $\mathrm{diag}\{1,1,-1,-1\} \cdot h_k$ and $[\Gamma_{k\mu}, \Gamma^\dagger_{k'\nu}] = \delta_{\mu\nu}\delta_{kk'}$. Finally, this calculation gives the $\mathcal{O}(S)$ zero-point energy fluctuations per site as a function of $\hat{\mathbf{e}}$,

$$E_{\mathrm{GS}}[\hat{\mathbf{e}}] = \frac{1}{N}\sum_k \sum_{\mu=1}^{2} \omega_{k,\mu}. \quad \text{(C6)}$$

This is the quantum analog of Eq. (A6). Evaluating $E_{\rm GS}$ numerically, we find that it is minimized for $\hat{\mathbf{e}}$ parallel to the cubic axes for either $\alpha > 1/2$ or $\alpha < 1/2$ (and at $\alpha = 1/2$). For example, $E_{\rm GS}$ is plotted for $\alpha = 0.45$ and $J_z = 1.5$, or alternatively for $\alpha = 0.6$ and $J_z = 0.5$ in Fig. 19 demonstrating that the magnetization points along the cubic axes in the stripy xy phases.

Whereas our linear spin wave calculation gives also the dispersion of the spin waves, $\omega_{k,\mu}$, it fails to show the opening of the gap of the Goldstone modes once the continuous symmetry is spoiled at $\alpha \neq 0$. A self-consistent spin wave calculation does account for the gap in the spin wave spectrum [6,36].

[1] W. Witczak-Krempa, G. Chen, Y. B. Kim, and L. Balents, Annu. Rev. Condens. Matter Phys. **5**, 57 (2014).
[2] L. Balents, Nature (London) **464**, 199 (2010).
[3] B. J. Kim, H. Jin, S. J. Moon, J.-Y. Kim, B.-G. Park, C. S. Leem, J. Yu, T. W. Noh, C. Kim, S.-J. Oh, J.-H. Park, V. Durairaj, G. Cao, and E. Rotenberg, Phys. Rev. Lett. **101**, 076402 (2008).
[4] B. J. Kim, H. Ohsumi, T. Komesu, S. Sakai, T. Morita, H. Takagi, and T. Arima, Science **323**, 1329 (2009).
[5] G. Jackeli and G. Khaliullin, Phys. Rev. Lett. **102**, 017205 (2009).
[6] J. Chaloupka, G. Jackeli, and G. Khaliullin, Phys. Rev. Lett. **105**, 027204 (2010).
[7] K. I. Kugel and D. I. Khomskii, JETP Lett. **15**, 446 (1972).
[8] Z. Nussinov and J. van den Brink, arXiv:1303.5922.
[9] A. Kitaev, Annal. Phys. **321**, 2 (2006).
[10] Y. Singh and P. Gegenwart, Phys. Rev. B **82**, 064412 (2010).
[11] Y. Singh, S. Manni, J. Reuther, T. Berlijn, R. Thomale, W. Ku, S. Trebst, and P. Gegenwart, Phys. Rev. Lett. **108**, 127203 (2012).
[12] S. K. Choi, R. Coldea, A. N. Kolmogorov, T. Lancaster, I. I. Mazin, S. J. Blundell, P. G. Radaelli, Y. Singh, P. Gegenwart, K. R. Choi, S.-W. Cheong, P. J. Baker, C. Stock, and J. Taylor, Phys. Rev. Lett. **108**, 127204 (2012).
[13] F. Ye, S. Chi, H. Cao, B. C. Chakoumakos, J. A. Fernandez-Baca, R. Custelcean, T. F. Qi, O. B. Korneta, and G. Cao, Phys. Rev. B **85**, 180403(R) (2012).
[14] H.-C. Jiang, Z.-C. Gu, X.-L. Qi, and S. Trebst, Phys. Rev. B **83**, 245104 (2011).
[15] R. Schaffer, S. Bhattacharjee, and Y. B. Kim, Phys. Rev. B **86**, 224417 (2012).
[16] J. Reuther, R. Thomale, and S. Trebst, Phys. Rev. B **84**, 100406(R) (2011).
[17] S. Chandra, K. Ramola, and D. Dhar, Phys. Rev. E **82**, 031113 (2010).
[18] M. E. J. Newman and G. T. Barkema, *Monte Carlo Methods In Statistical Physics* (Clarendon Press, Oxford, 1999).
[19] W. Janke, in *Computational Many-Particle Physics*, Lecture Notes in Physics Vol. 739, edited by H. Fehske, R. Schneider, and A. Weiße (Springer-Verlag, Berlin, 2008).
[20] C. J. Geyer, in *Computing Science and Statistics: Proceedings of the 23rd Symposium on the Interface*, edited by E. M. Keramidas (Interface Foundation, Fairfax Station, 1991).
[21] K. Hukushima and K. Nemoto, J. Phys. Soc. Jpn. **65**, 1604 (1996).
[22] C. C. Price and N. B. Perkins, Phys. Rev. Lett. **109**, 187201 (2012).
[23] C. C. Price and N. B. Perkins, Phys. Rev. B **88**, 024410 (2013).
[24] J. V. José, L. P. Kadanoff, S. Kirkpatrick, and D. R. Nelson, Phys. Rev. B **16**, 1217 (1977).
[25] A. M. Ferrenberg and R. H. Swendsen, Phys. Rev. Lett. **63**, 1195 (1989).
[26] J. D. Chodera, W. C. Swope, J. W. Pitera, C. Seok, and K. A. Dill, J. Chem. Theory Comput. **3**, 26 (2007).
[27] W. H. Press, S. A. Teukolsky, W. T. Vetterling, and B. P. Flannery, *Numerical Recipes 3rd Edition: The Art of Scientific Computing* (Cambridge University Press, New York, 2007).
[28] B. Efron, *The Jackknife, the Bootstrap and Other Resampling Plans* (SIAM, Philadelphia, 1982).
[29] C. L. Henley, Annu. Rev.Condens. Matter Phys. **1**, 179 (2010).
[30] G. H. Wannier, Phys. Rev. **79**, 357 (1950).
[31] P. W. Kasteleyn, J. Math. Phys. **4**, 287 (1963).
[32] V. Elser, J. Phys. A **17**, 1509 (1984).
[33] J. T. Chalker, P. C. W. Holdsworth, and E. F. Shender, Phys. Rev. Lett. **68**, 855 (1992).
[34] G. Baskaran, D. Sen, and R. Shankar, Phys. Rev. B **78**, 115116 (2008).
[35] S. R. White, Phys. Rev. Lett. **69**, 2863 (1992).
[36] G. Khaliullin, Phys. Rev. B **64**, 212405 (2001).
[37] R. Steinigeweg and W. Brenig, arXiv:1312.4954.
[38] T. Giamarchi, *Quantum Physics in One Dimension* (Oxford University Press, New York, 2004).
[39] H.-C. Jiang and L. Balents, arXiv:1309.7438.
[40] S. Trebst, P. Werner, M. Troyer, K. Shtengel, and C. Nayak, Phys. Rev. Lett. **98**, 070602 (2007).
[41] I. S. Tupitsyn, A. Kitaev, N. V. Prokof'ev, and P. C. E. Stamp, Phys. Rev. B **82**, 085114 (2010).
[42] J. Vidal, S. Dusuel, and K. P. Schmidt, Phys. Rev. B **79**, 033109 (2009).
[43] J. Vidal, R. Thomale, K. P. Schmidt, and S. Dusuel, Phys. Rev. B **80**, 081104 (2009).
[44] S. Dusuel, M. Kamfor, K. P. Schmidt, R. Thomale, and J. Vidal, Phys. Rev. B **81**, 064412 (2010).
[45] S. Dusuel, M. Kamfor, R. Orús, K. P. Schmidt, and J. Vidal, Phys. Rev. Lett. **106**, 107203 (2011).
[46] K. P. Schmidt, Phys. Rev. B **88**, 035118 (2013).
[47] M. Kamfor, S. Dusuel, J. Vidal, and K. P. Schmidt, Phys. Rev. B **89**, 045411 (2014).
[48] E.-G. Moon and C. Xu, Phys. Rev. B **86**, 214414 (2012).
[49] S. Sachdev, Phys. Rev. B **45**, 12377 (1992).
[50] I. Rousochatzakis, U. K. Rössler, J. van den Brink, and M. Daghofer, arXiv:1209.5895.
[51] I. Kimchi and A. Vishwanath, Phys. Rev. B **89**, 014414 (2014).
[52] I. Kimchi, J. G. Analytis, and A. Vishwanath, arXiv:1309.1171.
[53] E. K.-H. Lee, R. Schaffer, S. Bhattacharjee, and Y. B. Kim, Phys. Rev. B **89**, 045117 (2014).
[54] J. Nasu, T. Kaji, K. Matsuura, M. Udagawa, and Y. Motome, Phys. Rev. B **89**, 115125 (2014).

[55] S. B. Lee, E. K.-H. Lee, A. Paramekanti, and Y. B. Kim, Phys. Rev. B **89**, 014424 (2014).

[56] E. K.-H. Lee, S. Bhattacharjee, K. Hwang, H.-S. Kim, H. Jin, and Y. B. Kim, Phys. Rev. B **89**, 205132 (2014).

[57] M. Hermanns and S. Trebst, Phys. Rev. B **89**, 235102 (2014).

[58] K. A. Modic, T. E. Smidt, I. Kimchi, N. P. Breznay, A. Biffin, S. Choi, R. D. Johnson, R. Coldea, P. Watkins-Curry, G. T. McCandless, F. Gandara, Z. Islam, A. Vishwanath, J. Y. Chan, A. Shekhter, R. D. McDonald, and J. G. Analytis, arXiv:1402.3254.

[59] T. Takayama, A. Kato, R. Dinnebier, J. Nuss, and H. Takagi, arXiv:1403.3296.